

Identifying Coherence Across End-of-Century Montane Snow Projections in the Western United States

Justin M. Pflug^{1,2}, Sujay V. Kumar¹, Ben Livneh³, Ethan D. Gutmann⁴, Sudershan Gangrade^{5,6}, Shih-Chieh Kao^{5,6}

¹Hydrological Sciences Laboratory, NASA Goddard Space Flight Center, Greenbelt, Maryland

²Earth System Sciences Interdisciplinary Center, University of Maryland, College Park, College Park, Maryland

³Cooperative Institute for Research in Environmental Sciences, University of Colorado, Boulder, Boulder, Colorado

⁴National Center for Atmospheric Research, Boulder, Colorado

⁵Environmental Sciences Division, Oak Ridge National Laboratory, Oak Ridge, Tennessee

⁶Climate Change Science Institute, Oak Ridge National Laboratory, Oak Ridge, Tennessee

Corresponding author: Justin M. Pflug (jpflug@umd.edu)

Key points:

- The relationship between snow projections had similar patterns with increases in elevation in five montane domains
- Projection magnitude and spread were used to benchmark when and where end-of-century changes to SWE were larger than model disparity
- Model coherence can be used to identify the locations of greatest projection confidence, and where improvements would be most beneficial

Abstract:

Montane snowpack is a vital source of water supply in the Western United States. However, the future of snow in these regions in a changing climate is uncertain. Here, we use a large-ensemble approach to evaluate the consistency across 124 statistically downscaled snow water equivalent (SWE) projections between end-of-century (2076 – 2095) and early 21st century (2106 – 2035) periods. Comparisons were performed on dates corresponding with the end of winter (15 April) and spring snowmelt (15 May) in five western US montane domains. By benchmarking SWE climate change signals using the disparity between snow projections, we identified relationships between SWE projections that were repeatable across each domain, but shifted in elevation. In low to mid-elevations, 15 April average projected decreases to SWE of 48% or larger were greater than the disparity between models. Despite this, a significant portion of 15 April SWE volume (39 – 93%) existed in higher elevation regions where the disparities between snow projections exceeded the projected changes to SWE. Results also found that 15 April and 15 May projections were strongly correlated ($r \geq 0.82$), suggesting that improvements to the spread and certainty of 15 April SWE projections would translate to improvements in later dates. The results of this study show that large-ensemble approaches can be used to measure coherence between snow projections and identify both 1) the highest-confidence changes to future snow water resources, and 2) the locations and periods where and when improvements to snow projections would most benefit future snow projections.

40 **Plain Language Summary:**

41 A significant portion of the Western United State’s water originates from mountain
42 snowpack. This study combines a large set of snow projections generated using different
43 modeling approaches to determine 1) where snow projections agree, and 2) the proportion of
44 snow that falls within regions where end-of-century projections of snow disagree. Results show
45 that while a majority of the area in the interior Rocky Mountains and Washington Cascade
46 mountain range have snow projections that agree, most of the annual snow water supply exists in
47 the highest elevations where estimates of end-of-winter snowpack diverge. This study highlights
48 the similar patterns of snow projection disparities, and the locations where further research may
49 most improve our confidence in future snow water supplies.

50 **1. Introduction:**

51 Seasonal snow in mountainous terrain is a crucial source of water storage, providing runoff
52 throughout the spring and summer snowmelt periods for agriculture, human consumption,
53 industry, energy production, and ecosystems. In the Western United States, a majority of annual
54 runoff is sourced from snowmelt (Li et al., 2017), but the volume and timing of snowmelt will
55 change with projected changes to climate (e.g., Alder and Hostetler, 2019; Barsugli et al., 2020;
56 Fyfe et al., 2017; Gergel et al., 2017; Ghan and Shippert, 2006; Ikeda et al., 2021; Leung et al.,
57 2004; Li et al., 2017; López-Moreno et al., 2017; McCrary and Mearns, 2019; Qian et al., 2010;
58 Rasmussen et al., 2014; Rhoades et al., 2018b, 2018a; Ullrich et al., 2018). Siirila-Woodburn et
59 al. (2021) estimated that 78 – 94% of Western US regions in the second half of the century (2050
60 – 2099) will have 70% or larger declines to peak snow water equivalent (SWE), and annually-
61 persistent low snow conditions emerging within the next 35 – 60 years. Historical snow
62 observations in the Western U.S. have also confirmed climate change’s impact on the volume of
63 annual SWE accumulation, the frequency of snowfall and rainfall, and the timing of spring
64 snowmelt onset (Hamlet et al., 2007; Harpold et al., 2012; Kapnick and Hall, 2012; Mote et al.,
65 2018; Musselman et al., 2021).

66 Changes to the volume and timing of montane snowpack threaten local ecosystems and alter
67 how water is partitioned between the land surface, evapotranspiration, and streamflow (Barnett et

68 al., 2005; Hale et al., 2022; Harpold and Brooks, 2018; Musselman et al., 2017), making this
69 information crucial for operational and policy decisions. Despite this, projections of future snow
70 water resources are uncertain in montane regions. One of the greatest drivers of this uncertainty
71 is the mismatch in spatial scales between the spatial heterogeneity of snowpack and the scale of
72 climate projections. For instance, global climate models (GCMs) discretize the land surface at
73 spatial scales much coarser (e.g., 50 – 200 km) than the variability of the topography in mountain
74 terrain. These models commonly misrepresent the snow evolution that occurs in higher-elevation
75 and snow dominated terrain, which may account for a small areal fraction of a GCM grid cell,
76 but a large portion of that grid cell’s snow volume. Misrepresentations of the spatial
77 heterogeneity of snow and topography in the GCMs can also have key feedback on montane
78 climate through processes like snow albedo feedbacks (Walton et al., 2017), and meteorological
79 processes like mountain-pass air mixing, orographic gradients, rain shadows, and barrier jets
80 (e.g., Guan et al., 2016; Hughes et al., 2009; Lundquist et al., 2010).

81 Snow evolution is also sensitive to processes like air temperature gradients and terrain
82 shading, both of which occur at length-scales much smaller than the spatial resolution of GCMs
83 (Clark et al., 2011). To represent these processes, it is common practice to downscale climate
84 projections. To date, dynamic and statistical downscaling are the two most common downscaling
85 approaches. Dynamic downscaling leverages the use of weather prediction models to more
86 directly simulate the interactions between the coarser-scale climate projections and the
87 underlying terrain. This approach resolves local weather patterns in a way that is not strictly
88 correlated with local terrain features, but instead attempts to resolve the meteorological impacts
89 that could occur from the interconnectedness of the land-atmosphere system (Gutmann et al.,
90 2012; Minder et al., 2016; Walton et al., 2017). However, dynamic downscaling approaches are

91 computationally expensive, and often still misrepresent the land surface conditions, interactions
92 between the land surface and atmosphere, and the resulting local meteorological conditions in
93 mountainous terrain (e.g., Aas et al., 2017; Le Roux et al., 2018; Xue et al., 2014). In this study,
94 we focus on statistically downscaled snow projections which are less computationally expensive
95 and more common in practice. Statistical downscaling derives finer resolution meteorology using
96 the relationship between GCMs and reference meteorological datasets in historical periods (e.g.,
97 Abatzoglou and Brown, 2012; Hidalgo et al., 2008; Orłowsky et al., 2010; Pierce et al., 2014;
98 Wood et al., 2004). However, this approach assumes that the reference datasets are accurate
99 when in reality, there are often biases in these datasets, particularly in remote and high-elevation
100 montane regions (e.g., Currier et al., 2017; Lundquist et al., 2015; Wayand et al., 2013).

101 Statistical downscaling also assumes a static relationship between the GCM output and finer-
102 scale reference dataset, when this relationship could change in time with a changing climate.

103 Even if credible meteorological forcings are available, modeling decisions have impacts on
104 estimates of snow evolution in complex terrain (Chegwidden et al., 2019; Srikrishnan et al.,
105 2022). Most snow projections simulate snow using spatiotemporally continuous climate
106 projections. However, other approaches have used the delta-method (e.g., Barsugli et al., 2020;
107 Sofaer et al., 2017), where monthly or more-frequent perturbations are made to a historical
108 record of climate (e.g., 20 – 30 years) based on average projected changes to meteorological
109 variables (e.g., temperature, precipitation, etc.). This approach prescribes future simulations with
110 the interannual variability from the historical climate record, but more-explicitly relates the
111 difference in modeled state variables to average changes in meteorological conditions. Different
112 land surface and snow models are also subject to different parameterizations and modeling
113 decisions, such as rain and snow thresholding, canopy interception, wind-redistribution, and

114 liquid water percolation. These parameterizations cause snow simulations across different
115 models to diverge from each other (Essery et al., 2013; Jennings et al., 2018; Lumbrazo et al.,
116 2022; Pflug et al., 2019; Reynolds et al., 2021). In fact, some studies have documented that the
117 differences between snow models cause snow simulations to differ by greater amounts than
118 different meteorological forcing datasets (Kim et al., 2021; Mudryk et al., 2015).

119 Different combinations of GCMs, downscaling approaches, and modeling decisions can have
120 interconnected and cascading impacts on model estimates of snow evolution. This makes the
121 sensitivities and sources of disparities between projections using different modeling approaches
122 difficult to attribute. Studies that analyze sensitivities to different model decisions often use a
123 central model setup with limited and user-defined changes to modeling decisions like
124 downscaling techniques, process parameterizations, or spatial resolutions (Abatzoglou and
125 Brown, 2012; Alder and Hostetler, 2019; Barsugli et al., 2020; Gutmann et al., 2014; Hughes et
126 al., 2017). However, this could underestimate snow projection sensitivity by neglecting the
127 compounding or compensating impacts that different sets of modeling decisions have (Essery et
128 al., 2013; Raleigh et al., 2015). For example, a downscaling method that produces air
129 temperatures closer to 0°C for a longer winter period may exhibit different sensitivities to a set of
130 rain and snow partitioning functions than colder downscaled estimates of air temperature.
131 Unfortunately, investigating the full interaction between multiple sets of modeling decisions
132 often requires large numbers of simulations, which are computationally expensive for snow
133 simulations over long-term future periods and mountain-range spatial extents.

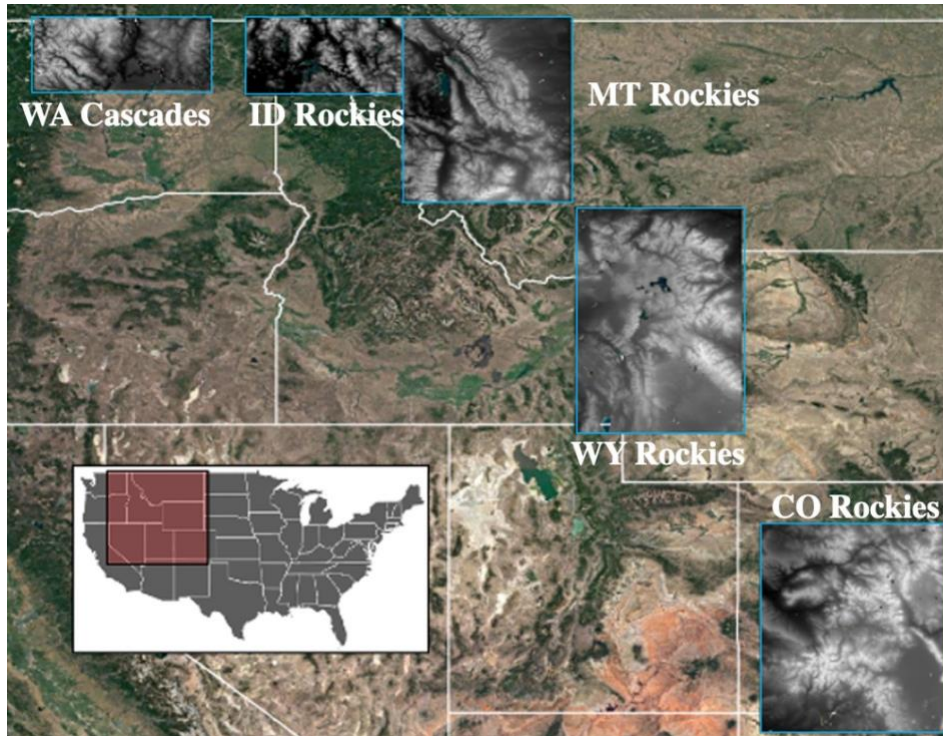
134 Rather than diagnosing the sources of disparities discussed above, this study focuses on
135 identifying the coherence, or the logical and consistent relationships between projected changes
136 to snow across six snow projection ensembles with disparate modeling approaches and decisions.

137 This approach is motivated by model intercomparison studies like the Earth System Model Snow
138 Model Intercomparison Project (ESM-SnowMIP; Krinner et al., 2018), which synthesizes
139 information from a wide set of data sources to draw conclusions about the similarity of modeled
140 hydrological states. Here, we focus on projected changes to end-of-century snow water resources
141 in five Western U.S. montane domains spanning a variety of snow climates (Section 2). By
142 benchmarking projected changes to SWE versus the disparities in SWE projections across
143 different modeling approaches, we ask: **1) where and when do projected changes to montane**
144 **snow water resources from different snow projections show consensus?, and 2) what**
145 **proportion of snow water resources exist in the regions with snow projection disparities?** In
146 doing so, we identify 1) the climate change signals of greatest confidence, and 2) the regions
147 where future improvements in model coherence would most improve future projections of snow
148 water resources.

149 **2. Domains and data**

150 **2.1. Model domains and historical snow reanalyses**

151 This project focused on five montane domains spanning a variety of snow climates and
152 latitudes in the Western United States (Figure 1). These regions were chosen to focus on high-
153 elevation domains with seasonal snowpack, with a special focus on the headwaters of snow
154 reservoirs for the Colorado River and Columbia River basins. These domains also overlapped
155 with known and proposed reintroduction habitat for snow-adapted species like the Canada lynx
156 (*Lynx canadensis*) and North American wolverine (*Gulo gulo luscus*). Snow projections in this
157 project were subset into five domains (Figure 1), labeled here as the Colorado (CO) Rockies
158 (~118,000 km^2), Wyoming (WY) Rockies (~104,000 km^2), Montana (MT) Rockies (~80,000
159 km^2), Idaho (ID) Rockies (~31,000 km^2), and Washington (WA) Cascades (~31,000 km^2).



160
 161 Figure 1. Western US montane study domains. Each domain is outlined in blue and is
 162 superimposed with a 0.01° grayscale elevation map.

163 Historical (1991 – 2021) SWE was defined from the Western United States UCLA Snow
 164 Reanalysis (Fang et al., 2022). This product generates SWE at daily timesteps and 16 arc-second
 165 (~500m) spatial resolution using an ensemble of snow simulations weighted towards annual
 166 observations of snow cover depletion from Landsat using a Bayesian smoother. This product is
 167 among the highest-accuracy estimates of SWE volume and distribution, demonstrating the
 168 capability to match in situ and airborne snow observations (Fang et al., 2020; Pflug et al., 2022).
 169 This data was used to provide an estimation of average historical snow distribution in each
 170 domain, that was independent from the snow projections compared here (Sections 2.2 and 2.3),
 171 as a basis for highlighting the proportion of each domain’s snow water resources that exist in
 172 regions with various levels of agreements and disparities across the snow projections.

173 **2.2. Novel montane snow projections**

174 Two snow projections were created for this study. A detailed description of these projections
175 can be found in Text S1. These projections were performed using a two-step modeling approach
176 which 1) developed a baseline simulation representative of snow evolution in a historical period
177 between 1995 and 2016 using forcing downscaled from MERRA2 (Gelaro et al., 2017) with
178 additional precipitation calibration, and 2) perturbed the MERRA2 baseline simulation with
179 future climate-change signals. While straightforward, this change-factor approach (also termed
180 the *delta method*) is a reliable approach for determining hydrological and ecological climate
181 sensitivities (Barsugli et al., 2020; Sofaer et al., 2017). In this study, future climate change
182 signals were derived from NASA Earth Exchange Global Daily Downscaled Projections (NEX-
183 GDD-CMIP6; Thrasher et al., 2022), which downscaled climate projections from the Coupled
184 Model Intercomparison Project phase 6 (CMIP6; Eyring et al., 2016) using the popular bias
185 correction spatial disaggregation (BCSD) approach (Wood et al., 2004) and reference historical
186 meteorological data from the Global Meteorological Forcing Dataset (GMFD; Sheffield et al.,
187 2006). Readers are referred to Thrasher et al. (2022) and Wood et al. (2004) for more
188 information on NEX-GDDP-CMIP6 and BCSD, respectively.

189 Using variogram analysis, we determined that the interannual variability in domain-mean
190 winter air temperature and precipitation for both the historical snow simulation and NEX-GDDP-
191 CMIP6 data plateaued for 14 – 18 year periods (e.g., Subyani, 2019) (Text S1). Beyond 18 years,
192 the change to domain mean temperature and precipitation were more driven by climate trends.
193 To be conservative, we partitioned the historical and future climate records into 20-year
194 windows. Since the CMIP6 “historic” data record runs from January 1950 to December 2014, the
195 20-year historical period for this study spanned from October 1994 to September 2014 (water
196 years 1995 to 2014). We then partitioned 20-year increments forward in time from the historic

197 record. Here, we focus on 20-year data records from an early 21st century period (2016 – 2035)
198 and end-of-century period (2076 to 2095). Monthly maps of change-signals in air temperature,
199 specific humidity, shortwave radiation, longwave radiation, wind speed, surface pressure, and
200 precipitation were then calculated for both the early 21st century and end-of-century periods from
201 the NEX-GDDP-CMIP6 data in those periods, relative to the historical period.

202 Finally, SWE projections were performed using two different approaches. First, model forcing
203 from the 20-year historical simulations between 1995 and 2014 was perturbed with average
204 monthly 0.01° climate change signals aggregated from the NEX-GDDP-CMIP6 data in the early
205 21st century and end-of-century periods. This simulation is referenced in this manuscript by
206 NEX6-C (“C” indicating that climate perturbations were performed in the 20-year *continuous*
207 simulation). The second simulation used the median forcing aggregated at daily timesteps for
208 each grid cell over the 20-year historical period. This simulation was then perturbed using the
209 same monthly climate change signals from NEX-GDDP-CMIP6. This simulation is referenced
210 by NEX6-M (“M” indicating that simulations were performed using 20-year *median* forcing).

211 The difference between the NEX6-C and NEX6-M simulations, which were perturbed using
212 the same climate change signals, were indicative of uneven climate change impacts on subsets of
213 years. For example, grid cells where NEX6-C projections that had end-of-century projected SWE
214 decreases that were larger than NEX6-M projections indicated that climate impacts on SWE in
215 these grid cells were disproportionately large in low snow years, as compared to years with
216 average snow conditions. This is discussed more in the study Results (Section 4) and Discussion
217 (Section 5). More information on the NEX6-M and NEX6-C snow projections can be found in
218 Text S1.

219 **2.3. Similarities and differences across novel and existing snow projections**

220 The snow projections discussed in Section 2.2 were compared with four additional
221 statistically-downscaled snow projections from the literature (Abatzoglou et al., 2014; Brekke et
222 al., 2013; Kao et al., 2022a; Vano et al., 2020). Information on each of these snow projections,
223 and the citations discussing each can be found in Table 1. Each snow projection dataset was
224 labeled using an acronym representative of the combination of the statistical downscaling and the
225 CMIP phase (Table 1). However, the commonalities and differences in modeling decisions
226 among the snow projection datasets go beyond the differences in CMIP phases and downscaling
227 approaches. For example, although three projection datasets use CMIP6 projections and three use
228 CMIP5 projections, identical sets of GCMs are only used by 1) NEX6-M and NEX6-C, and 2)
229 LOCA5 and BCSD5. More information on the GCMs used by each projection dataset can be
230 found in Text S2. Half of the datasets use the BCSD downscaling (NEX6-M, NEX6-C, and
231 BCSD5). However, four unique reference datasets are used to downscale these climate
232 projections compared here, all of which are at different spatial resolutions. Although snow
233 projections are generated using only two different land surface models, different model
234 parameterizations and calibrations were used. Here, the cascading differences in the projections,
235 GCMs, and downscaling decisions in Table 1 alter the model forcing applied for each model
236 ensemble member.

237 As discussed in Section 1, differences in modeling methods make the differences across
238 projection datasets difficult to attribute, and often even more difficult to determine what
239 approaches are better and worse than others. For example, assuming that the differences in the
240 snow projections compared here can be attributed to only the GCMs used by the snow
241 projections (Text S2), and the degrees of freedom in modeling decisions listed in Table 1 (four
242 statistical downscaling approaches, four reference datasets, two time discretizations, and two

243 land surface models), a full sensitivity analysis covering all possible combinations of GCMs and
244 modeling decisions would result in 3,520 separate projections. Given this, we hypothesize that
245 the snow and climate research communities may benefit most from studies that evaluate where
246 and when disparate modeling decisions approach common results, and the consequences of
247 uncertainties in locations where models disagree the most. This study focuses on six snow
248 projection methodologies outputting 124 different snow projections. Our approach for comparing
249 these projections is covered in Section 3 below.

250 Table 1. Selection of the differences between the snow projection datasets compared in this
 251 study. More information on these projections, and how the NEX6-M and NEX6-C projections
 252 were generated can be found in Text S1 and Text S2.

Dataset	Climate forcing	Downscaling			Climate perturbation	Land surface model
		Statistical approach	Reference dataset	Resolution		
NEX6-M (Section 2.2)	CMIP6; Climate Model Intercomparison Project, phase 6	BCSD; Bias Correction and Spatial Disaggregation (Wood et al., 2004)	GMFD; Global Meteorological Forcing Dataset (Sheffield et al., 2006)	1/100°	Delta method (Sofaer et al., 2017)	Noah-MP (Niu et al., 2011)
NEX6-C (Section 2.2)	CMIP6	BCSD	GMFD	1/100°	Delta method	Noah-MP
DBCCA6 (Kao et al., 2022)	CMIP6	DBCCA; Double Bias Corrected Constructed Analogues (Werner and Cannon, 2016)	Daymet (Thornton et al., 2021)	1/24°	Continuous	VIC; Variable Infiltration Capacity model (Liang et al., 1994)
BCSD5 (Brekke et al., 2013)	CMIP5; Climate Model Intercomparison Project, phase 5	BCSD	Maurer et al. (2002)	1/8°	Continuous	VIC
LOCAS (Vano et al., 2020)	CMIP5	LOCA; Localized Constructed Analogues (Pierce et al., 2014)	Livneh et al. (2015)	1/16°	Continuous	VIC
MACA5 (Abatzoglou et al., 2014)	CMIP5	MACA; Multivariate Adaptive Constructed Analogs (Abatzoglou and Brown, 2012)	Livneh et al. (2015)	1/16°	Continuous	VIC

253 3. Methods

254 This study was designed to investigate 1) the shift in end-of-century projected SWE within
255 each snow projection dataset, and 2) the disparity in projected changes to SWE between the
256 projection datasets. Our comparisons were limited to the RCP 4.5 (CMIP5) and SSP2-4.5
257 (CMIP6) emission scenarios, which represent moderate, “middle-of-the-road” estimates of future
258 emissions, global populations, and climate adaptation inequities (IPCC, 2021). To compare
259 continuous snow projections more fairly versus the 20-year median simulations from NEX6-M
260 (Section 2.2), median SWE was calculated at the grid cell-level for each projection dataset across
261 early 21st century (2016 – 2035) and end-of-century (2076 – 2095) periods. Here, we focused on
262 the projected change to SWE on 15 April and 15 May. The 15 April date was chosen to
263 correspond with a period that was near the conclusion of the early 21st century winter snow
264 accumulation season, but late enough to ensure that the date of domain maximum SWE volume
265 occurred prior to that date. The 15 May date was selected to correspond with the period
266 approximately midway through the melt season based on the snow reanalysis dataset (Section
267 2.1). In the Western U.S., these dates (15 April and 15 May) correspond with reference dates
268 used for assessing streamflow, water infrastructure management decisions, and snow refugia
269 (e.g., Barsugli et al., 2020; Koster et al., 2010; Ray et al., 2020).

270 SWE projections for each period (2016 – 2035 and 2076 – 2095, 15 April and 15 May) were
271 discretized in space using the native spatial resolution for each dataset (Table 1). Each projection
272 dataset was also disaggregated to a 0.01° grid using nearest-neighbor downscaling. Comparisons
273 between these two spatial discretizations allowed comparisons between the snow projection
274 datasets on a common grid, and highlighted how different representations of the land surface
275 terrain and vegetation impacted the physical processes that influenced snow evolution. For

276 example, snow projections at coarser resolutions can smooth features like mountain peaks, which
 277 although small in areal extent, are colder than their surroundings and may therefore be less
 278 sensitive to projected increases in future temperatures.

279 The spread of SWE projections for each dataset (Table 1), 20-year period (early 21st century
 280 and end-of-century), and date (15 April and 15 May) was prescribed by the spread of GCMs
 281 (Figure 2). Provided the length of time between the early 21st century and end-of-century
 282 periods, we expect the differences in the GCM ensemble spread between the two periods to be
 283 driven more by differences in GCM physics than internal variability (Hawkins and Sutton, 2009;
 284 Lehner et al., 2020). We started by comparing the difference in the distributions of SWE
 285 between the two 20-year periods at each 0.01° disaggregated grid cell (Figure 2a). We used a
 286 non-parametric approach, wherein distributions of SWE with no overlap indicated the largest
 287 signal of change, and distributions of SWE with high degrees of overlap indicated little-to-no
 288 change. This measure represented how large and certain SWE changes were over time provided
 289 the spread in SWE estimates from the GCMs in each period. The non-parametric approach we
 290 used was motivated by the Mann-Whitney U test,

$$291 \quad U_1 = n_1 n_2 + \frac{n_1(n_1+1)}{2} - \sum R_1, \quad (1)$$

$$292 \quad U_2 = n_1 n_2 + \frac{n_2(n_2+1)}{2} - \sum R_2, \quad (2)$$

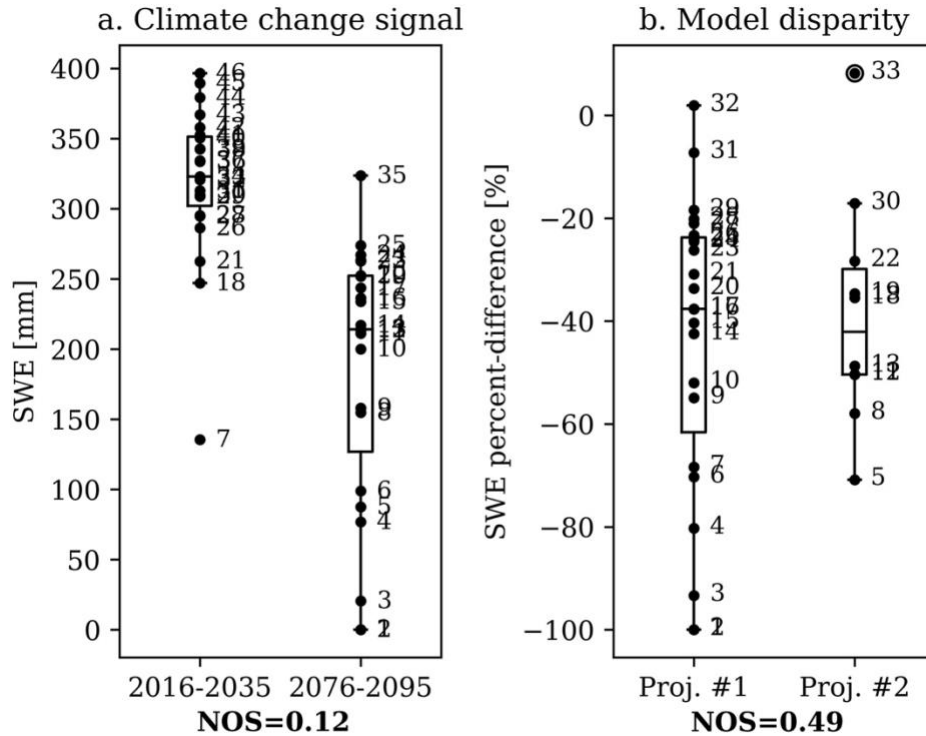
293 where subscripts 1 and 2 indicate the early 21st century (2016 – 2035) and end-of-century (2076
 294 – 2095) periods, n indicates the number of GCMs, and R indicates the rank of each GCM, ranked
 295 from lowest to highest values, including both 20-year periods (Figure 2a, numbering). The
 296 difference between U_1 and U_2 represents the degree of overlap in the SWE distributions between
 297 the two periods. For example, if projected changes to climate cause the end-of-century
 298 distribution of SWE to fall completely outside of the SWE distribution from the early 21st

299 century, then the disparity between the U values would be large, as U_2 and U_1 use the lowest-
300 possible and highest-possible sum of ranks, respectively ($\sum R_1 \gg \sum R_2$). Conversely, grid cells
301 with little-to-no change in SWE would approach similar sums of ranks ($\sum R_1 \approx \sum R_2$), and
302 similar U values.

303 A similar approach was used to evaluate the disparity between projected changes to SWE
304 (Figure 2b). Specifically, for each 0.01° grid cell and snow projection dataset, the SWE percent-
305 difference was calculated for each GCM between the early 21st century and end-of-century
306 periods. To fairly compare snow projections with different numbers of GCMs (n), we calculated
307 a Normalized Overlap Statistic (NOS)

$$308 \quad NOS = \frac{\min[U_1, U_2]}{U_1 + U_2}, \quad (3)$$

309 where NOS approaching 0.0 indicates a large difference in the distribution of SWE between the
310 two periods, and NOS approaching 0.5 indicates little-to-no difference. The NOS statistic was
311 calculated at each 0.01° grid cell for 1) each snow projection dataset using SWE between the
312 early 21st century and end-of-century periods (e.g., Figure 2a), and 2) for all combinations of two
313 snow projection datasets using the SWE percent-change between the early 21st century and end-
314 of-century periods (e.g., Figure 2b). The NOS statistic is discussed more in Section 5.



315
 316 Figure 2. Conceptual demonstration of, a) the climate change signal on the SWE distribution
 317 over time for a single snow projection, and b) the difference in projected changes to SWE
 318 between two snow projections. Both subplots represent comparisons at a single 0.01° grid cell,
 319 with each scatter point representing a different GCM. Labels represent the ranks (R from
 320 Equations 1 and 2), and the NOS (Equation 3) for each comparison is labeled beneath the plot.

321 Finally, this study found that projected changes to SWE exhibited relationships with elevation
 322 in each domain. Therefore, statistics were aggregated over 100 m elevation bands. For each
 323 elevation band, we calculated the median and spread of 1) SWE percent-changes between the
 324 early 21st century and end-of-century periods, 2) NOS for changes to SWE in time for all
 325 projection datasets (termed *climate change signal*), 3) NOS for the differences to the projected
 326 changes to SWE between all combinations of two snow projections (termed *model disparity*),
 327 and 4) SWE from the Western US snow reanalysis (Section 2.1). We recognize that climate
 328 change signals (Figure 2a) and model disparities (Figure 2b) calculated using the NOS statistic
 329 are not independent of each other. Instead, these statistics were used together to benchmark the
 330 behavior of snow projections in time, relative to the disparities across the full set of snow

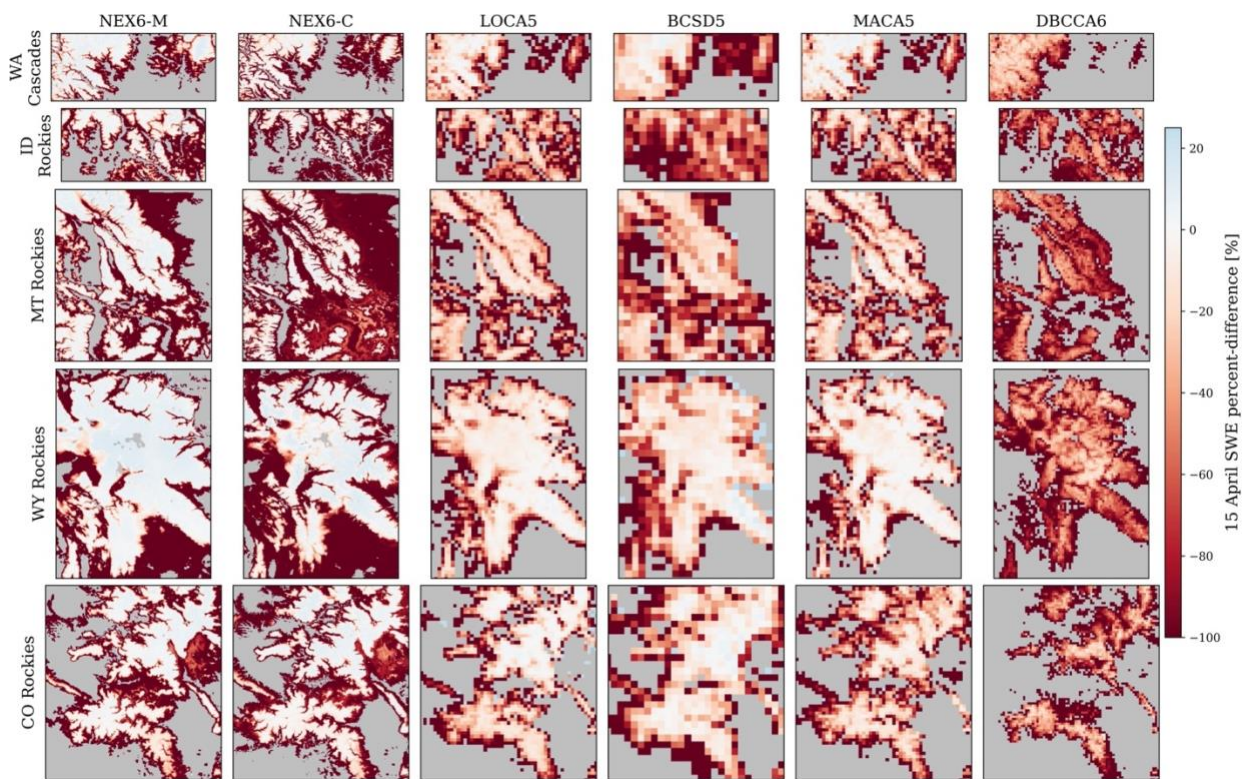
331 projections. For example, elevations with model disparities (Figure 2b) that approached large
332 NOS values represented SWE percent-changes that could not be easily differentiated between the
333 different snow projections. If those same elevations also had climate change signals with low
334 NOS values (e.g., Figure 2a), then the degree of change to SWE over time was large but in
335 agreement across the different snow projection datasets. Here, by comparing these four data
336 sources at each elevation band, we determined the volume of snow losses projected by each
337 snow projection dataset, the SWE climate change signal relative to the disparity across models,
338 and the amount of snow that historically existed in each elevation band. Together, these metrics
339 were used to determine where *coherence*, or logical and consistent relationships across snow
340 projections using disparate modeling approaches, and the portion of each domain's snow that
341 falls within regions where snow projections agree and disagree.

342 **4. Results**

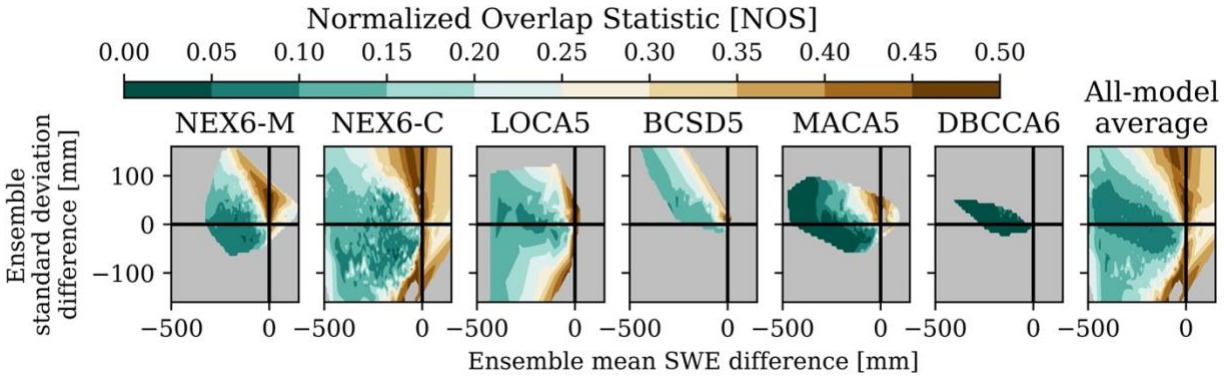
343 **4.1. SWE projection comparisons, and relationships with elevation**

344 Median projected changes to end-of-century SWE are shown for each domain and projection
345 dataset on 15 April and 15 May in Figure 3 and Figure S1, respectively. The most visible
346 differences between the snow projections in each domain were 1) differences in 2016 – 2035
347 snow extents (Figure 3, grid cells showing any projected change), and 2) disparities in the sign
348 (positive/negative) and magnitude of projected changes to snow at the highest elevations of each
349 domain. The Normalized Overlap Statistic (NOS, Equation 3) was able to highlight the
350 similarities and differences in SWE projections, both within a given snow projection dataset over
351 time (e.g., Figure 2a), and across multiple snow projection datasets (e.g., Figure 2b). For
352 example, Figure 4 displays the 15 April NOS calculated across all grid cells in the WA Cascades
353 domain. Contours in Figure 4 show the NOS values relative to the change in ensemble mean

354 SWE and SWE standard deviation between the early 21st century and end-of-century periods for
 355 each projection. Relative to the NEX6-M, NEX6-C, and MACA5 projections which projected
 356 both decreases and increases to end-of-century mean SWE, the BCSD5 and DBCCA6 models
 357 were dominated by grid cells with decreases to mean SWE and increases to the standard
 358 deviation of SWE across the GCMs. Despite this, the NOS exhibited similar patterns with
 359 changes to the mean and spread of SWE for each of the snow projection datasets (Figure 4, all-
 360 model average), with the smallest degree of overlap between early 21st century and end-of-
 361 century SWE (smallest NOS) occurring for grid cells with mean SWE decreases of 50 mm or
 362 more, and changes to SWE standard deviation between -50 mm and +100 mm.



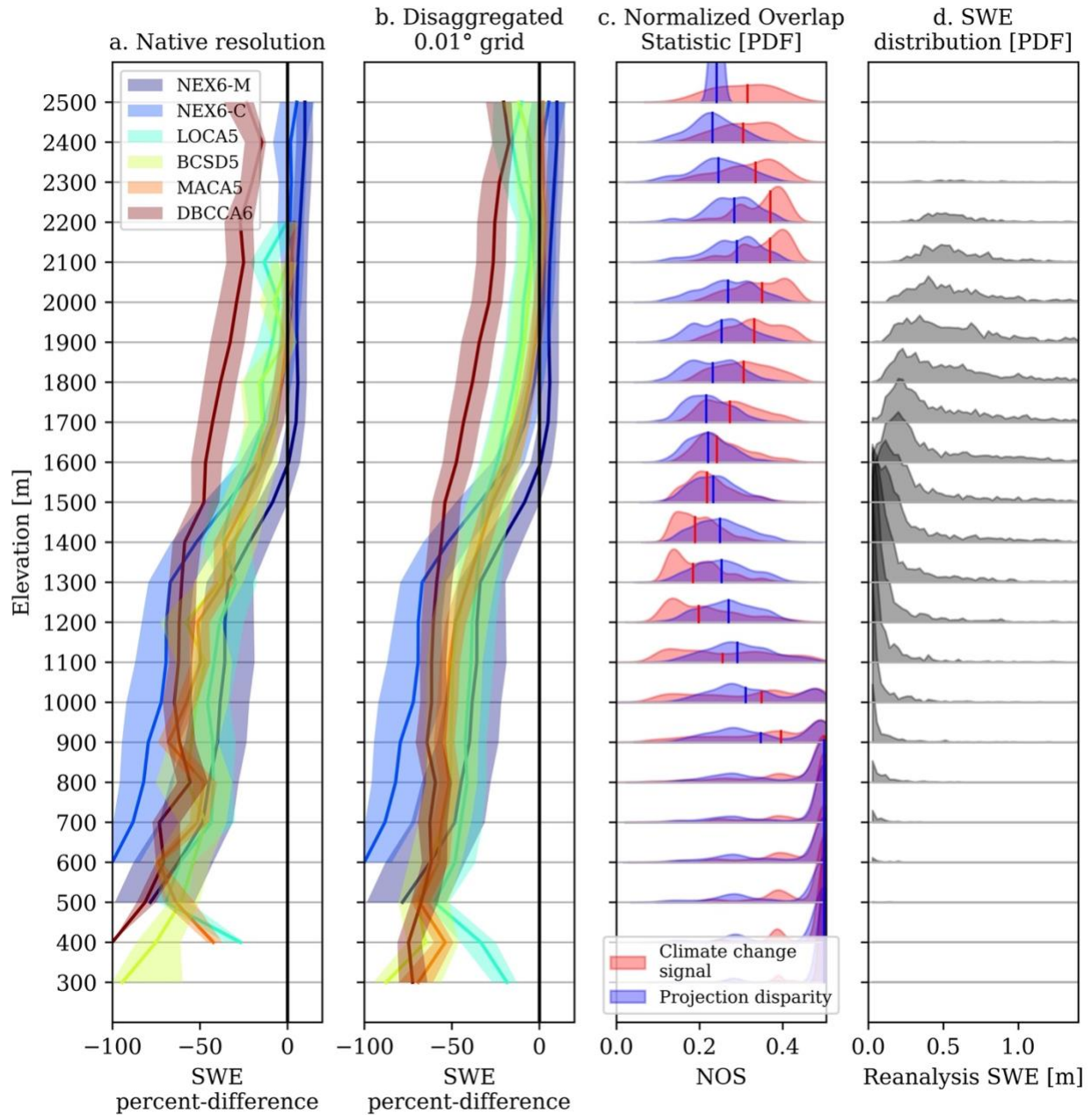
363
 364 Figure 3. Spatial plots of median percent changes to 15 April SWE between an early 21st century
 365 (2016 – 2035) and end-of-century (2076 – 2095) period for five montane domains (rows) and six
 366 snow projection datasets (columns).



367
 368 Figure 4. NOS (Equation 3) calculated between the early 21st century and end-of-century 15
 369 April periods in the WA Cascades. Each subplot (projection dataset) is contoured based on the
 370 NOS values, ensemble mean SWE difference (x-axis), and ensemble SWE standard deviation
 371 difference (y-axis).

372 Projected percent-changes to 15 April SWE and the NOS statistic exhibited similar trajectories
 373 with increases in elevation in each domain (Figure 5, Figures S2 – S10). NEX6-C simulations
 374 commonly had the largest (in percent-difference) projected decreases to end-of-century snow at
 375 the lowest elevations of each domain, with median SWE changes between -87% and -100%, on
 376 average. Although the modeling approaches for the NEX6-M and NEX6-C projections were
 377 similar (Section 2.2), NEX6-M projected changes to SWE were among the most optimistic snow
 378 projections, with projected changes to SWE between -64% and -91% for the same low-elevation
 379 regions. At higher elevations, NEX6-M and NEX6-C simulations both exhibited steep gradients
 380 in SWE projections with changes in elevation. For example, in the WA Cascades domain,
 381 decreases to end-of-century SWE for both the NEX6-M and NEX6-C datasets decreased by
 382 approximately 12% for every 100 m increase in elevation between approximately 1350 and
 383 1750m (Figure 5a). This gradient appeared in every domain for the NEX6-M and NEX6-C
 384 projections, varying in slope from approximately 8% (MT Rockies) to 17% (WY Rockies) per
 385 every 100 m in elevation. At elevations above these sharp gradients, NEX6-M and NEX6-C
 386 ensemble-medians projected either little-to-no change or increases to 15 April end-of-century
 387 SWE. Although the elevation at which median SWE first projected increases to 15 April SWE

388 differed between the NEX6-M and NEX6-C projections, projected changes to SWE at the
 389 highest elevations of each domain typically agreed to within 5%.

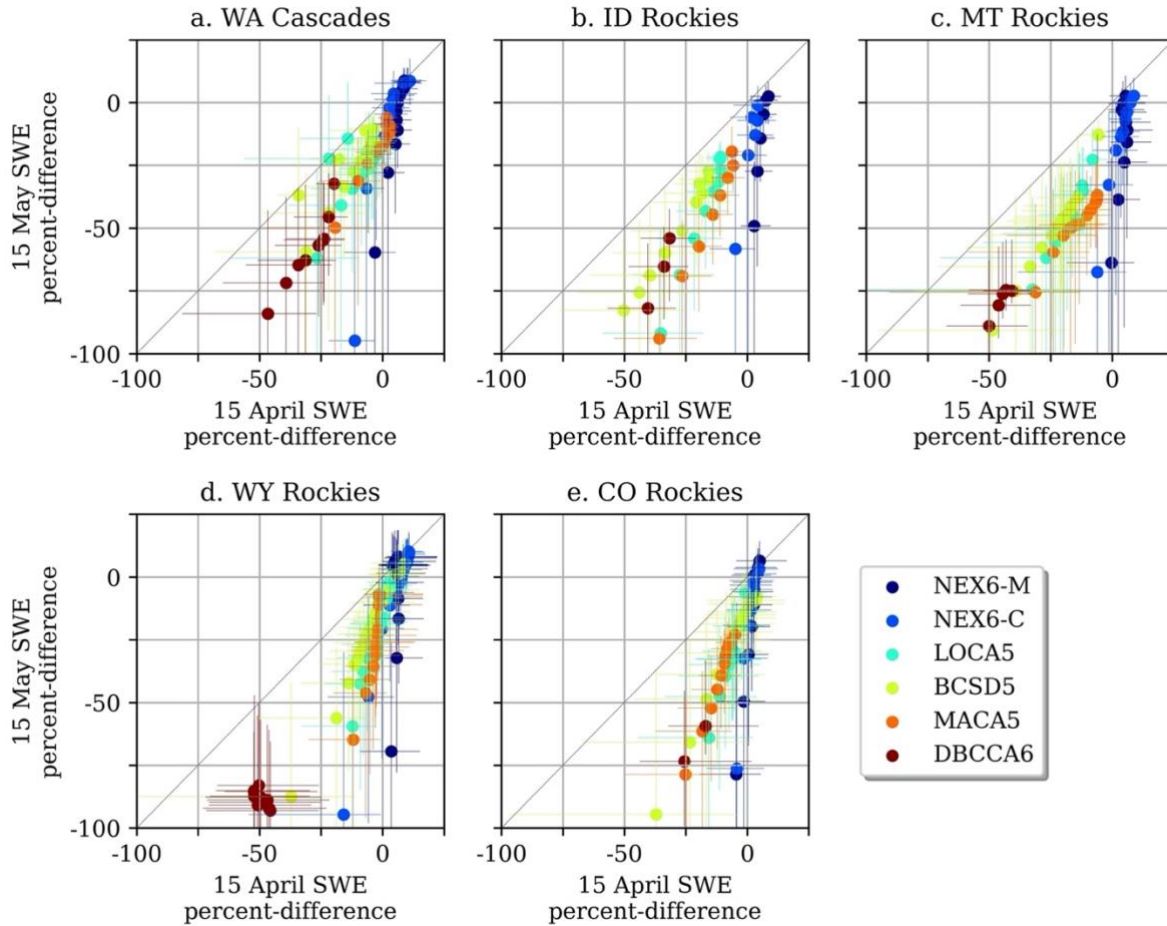


390
 391 Figure 5. 15 April snow projections for the WA Cascades domain aggregated across 100 m
 392 elevation bands (y-axis). Subplots show the GCM median and interquartile spread of SWE
 393 percent-change from the native-resolution snow projection datasets (a), and the same statistics
 394 for the snow projection datasets disaggregated to 0.01° (b). The remaining subplots show the
 395 distribution and median of the NOS climate change and projection disparity signals (c), and the
 396 distribution of SWE from the snow reanalysis (d).

397 As opposed to the NEX6-M and NEX6-C projections, end-of-century 15 April SWE
398 projections changed more gradually with increases in elevation for the LOCA5, BCSD5,
399 MACA5, and DBCCA6 projections (Figure 5a, Figures S2 – S10, Table S1). At the lowest
400 elevations of each domain, these projections typically estimated 15 April SWE decreases that fell
401 near or within the bounds estimated from the NEX6-M and NEX6-C projections. Then, with
402 every 100 m increase in elevation, 15 April SWE decreases changed between 2% and 4%, on
403 average, for the LOCA5, BCSD5, and MACA5 projections. 15 April SWE for these datasets
404 were either projected to decrease, or had smaller projected increases to SWE than the NEX6-M
405 and NEX6-C projections at the highest elevations of each domain. Here, the DBCCA6 snow
406 projections were consistently more pessimistic than the other projection datasets (Figure 5). In
407 fact, in no domain did the DBCCA6 dataset project increases to 15 April SWE across any
408 elevation band, and at the highest-elevations, DBCCA6 projected SWE losses ranging from -
409 21% (CO Rockies) to -48% (WY Rockies).

410 As compared to the 15 April date, the SWE percent-difference on 15 May had larger projected
411 decreases. This was expected since SWE projections on 15 May were influenced by both winter
412 SWE change signals, like transitions from snowfall to rainfall and earlier snowmelt onset, in
413 addition to increased rates of spring snowmelt driven by end-of-century increases in spring
414 snowmelt energy and thinner snowpacks that melted more readily. The relationships between the
415 SWE percent change and elevation discussed above exhibited similar patterns on both 15 April
416 and 15 May. However, these patterns were shifted up in elevation with spring snowmelt. This
417 caused nearly-linear relationships between the 15 April and 15 May SWE projections at common
418 elevation bands (Figure 6), the slope of which was driven in large part by the 15 April SWE
419 projections. For example, for the NEX6-M and NEX6-C projections, each domain exhibited

420 decreases to end-of-century SWE that were 40% or greater at the lowest elevations, and little-to-
421 no (-10 to +10%) changes to SWE at the highest elevations (e.g., Figure 3 and Figure 5).
422 Between 15 April and 15 May, the pattern of 15 April SWE changes were shifted up in elevation
423 by approximately 500 m (Figure S2), causing: 1) 15 May snow disappearance at elevations with
424 15 April projected SWE losses exceeding approximately 20%, 2) changes to 15 May SWE
425 between -25% and -100% for many mid-elevation grid cells that experienced little-to-no
426 decreases in 15 April SWE, and 3) little-to-no change in 15 May SWE at the highest-elevation
427 grid cells in each domain (Figure 6). Put simply, datasets that exhibited sharper gradients in 15
428 April SWE changes with elevation resulted in larger changes between 15 April and 15 May SWE
429 projections as these patterns were propagated up in elevation. This was also the case for the
430 LOCA5, BCSD5, and MACA5 projections in the WY Rockies domain (Figure 6d), which had
431 sharper gradients in SWE projections at elevations between 1500 and 2500 m (Figure S7 and
432 Table S1). However, in all other domains, these projections exhibited more gradual changes to
433 SWE projections with elevation (Figure 5, Figure S3, Figure S5, and Figure S9), resulting in a
434 smaller change to SWE percent-difference between 15 April and 15 May as the climate change
435 signal was propagated up in elevation. These results demonstrate hysteresis between snow
436 projections on 15 April and 15 May, showing that the coherence between different snow
437 projections in the snowmelt season is dependent on the coherence between models at the end-of-
438 winter period. This is discussed more in Section 5.



439
 440 Figure 6. Projected changes to SWE for each dataset (colors) and domain (subplots) on 15 April
 441 (x-axis) and 15 May (y-axis). The median and interquartile range of projections over 100 m
 442 elevation bands are shown by the scatter points and whiskers, respectively. Plotted data only
 443 includes elevation bands where 15 May median SWE was greater than zero.

444 Disaggregating each projection’s grid cells into a 0.01° grid resulted in smoother gradients to
 445 SWE percent-changes with elevation (e.g., Figure 5b). This approach also extrapolated SWE
 446 percent-change estimates to higher elevations that were sometimes unable to be represented by
 447 the coarser-scale snow projections. Overall, this extrapolation to higher elevations resulted in
 448 coarser-scale projections that increased in similarity with finer-scale snow projections. For
 449 example, in the ID Rockies domain, BCSD5 projections ($1/8^\circ$) were unable to resolve grid cells
 450 at elevations of 2200 m or higher. At its highest native-resolution elevation band (2050 –
 451 2150m), the BCSD5 dataset projected a 38% decrease to 15 May SWE, on average (Figure S4a).

452 However, preferentially sampling only those BCSD5 pixels that overlapped the highest elevation
453 band captured by the 0.01° digital elevation model (2250 – 2350 m) only had a 27% decrease in
454 15 May SWE at the end-of-century period (Figure S4b). This SWE projection agreed closer with
455 the LOCA5 (22% decrease) and MACA5 (20% decrease) estimates at the same elevations.

456 **4.2. Snow classes with coherent snow projection patterns**

457 As noted in Section 4.1, projected changes to end-of-century SWE exhibited similar patterns
458 between the different snow projection datasets. While these patterns occurred at different
459 elevations across each domain, these relationships could be used to identify regions with similar
460 climate impacts and systematic differences across the projections. Using the NOS statistic as a
461 metric for both climate change signals (Figure 2a) and the disparity across models (Figure 2b),
462 six unique snow signals were classified. Of these six classes, five appeared in every domain, and
463 appeared in the same sequence with increases in elevation. These snow classes, listed from
464 lowest to highest elevations, included the following:

465 **Class 1 (C1). Ephemeral snow cover:** Different snow projections disagreed on the occurrence
466 of 15 April snow in the first 20-year period (2016 – 2035), but end-of-century projections
467 agreed that snow disappeared. This snow class covered the lowest-elevation portions of each
468 domain.

469 **C2. Seasonal snow line:** This class included low-elevation and thin snowpack, but contained
470 enough snow volume to calculate the overlap in SWE distributions between the early 21st
471 century and end-of-century periods (Figure 2a), and the overlap between SWE projections
472 across the different datasets (Figure 2b).

473 **C3. SWE decreases > model disparity:** This snow class had little overlap between SWE
474 distributions from the early 21st century and end-of-century periods. On average, differences in

475 SWE between the early 21st century and end-of-century periods exceeded the disparities
476 across the SWE projections. In other words, the NOS for the climate change signal (Figure
477 2a) was smaller than the NOS for the model disparity (Figure 2b).

478 **C4. Model disparity > changes to SWE:** In this snow class, the differences across different
479 snow projections were greater, on average, than the difference in SWE distributions between
480 the early 21st century and end-of-century periods. These grid cells often had disagreements
481 about the direction (positive or negative) of projected changes to SWE.

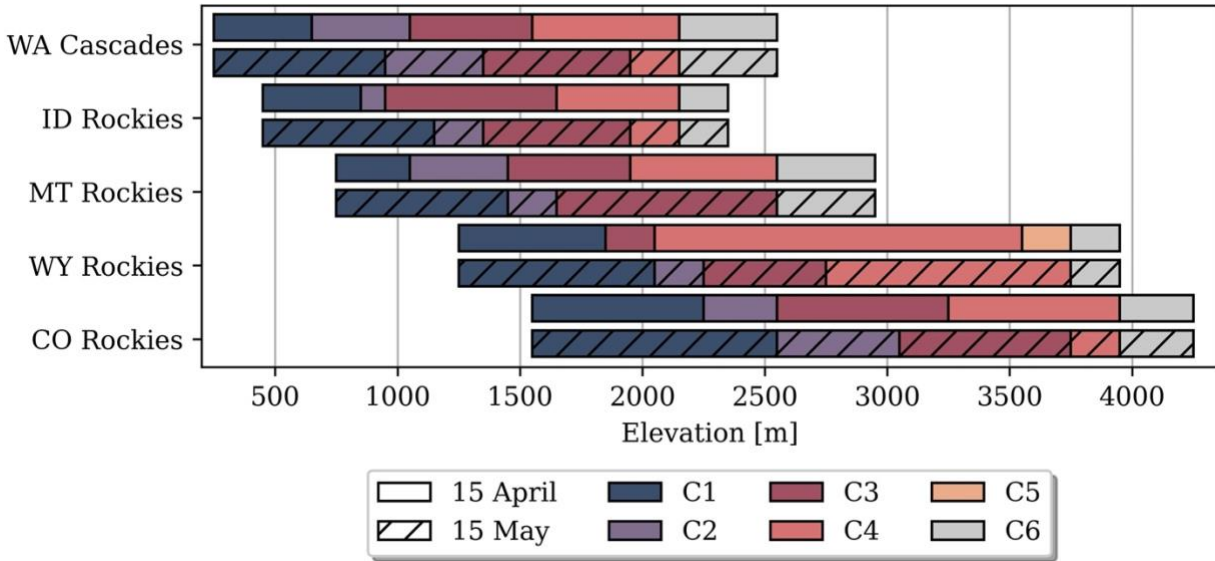
482 **C5: SWE increases > model disparity:** This class had projected increases to SWE with
483 differences between the early 21st century and end-of-century SWE distributions that were
484 larger, on average, than the difference in SWE projections across the different datasets.

485 **C6: Elevations smoothed by coarser resolutions:** The capability to resolve the highest peaks
486 was limited by the spatial resolution of the projection datasets. This class represented
487 elevation bands (calculated at 0.01° resolution) that couldn't be resolved by all snow
488 projection datasets.

489 The grid cells that fell within each of the classes listed above were based on the climate
490 change signals and model disparities calculated from the NOS statistic. In the WA Cascades
491 domain (Figure 5c), elevations spanning 250 – 650 m had ephemeral snow and disagreements in
492 snow extents between the projection datasets in the early 21st century (snow class C1). 15 April
493 snow cover was more common for elevations between 650 – 1050 m, which had large projected
494 decreases to end-of-century SWE, resulting in NOS statistics that could begin to resolve the
495 disparity between models and the climate change signal (C2). At elevations just above this (1050
496 – 1550 m), SWE was projected to decrease by approximately 52%, on average, with relatively
497 small variability across the snow projection datasets. This caused the early 21st century and end-

498 of-century SWE distributions to separate to a degree that was larger than the disparity in SWE
499 projections across different projection datasets (C3). Finally, the large spread and differing
500 directions (positive/negative) of projected changes to SWE at elevations greater than 1550 m
501 caused the disparity across models to exceed the average projected changes to SWE (C4). This
502 included the highest-elevation grid cells (2150 m and higher) that were unable to be resolved by
503 the coarser-resolution snow projections (C6).

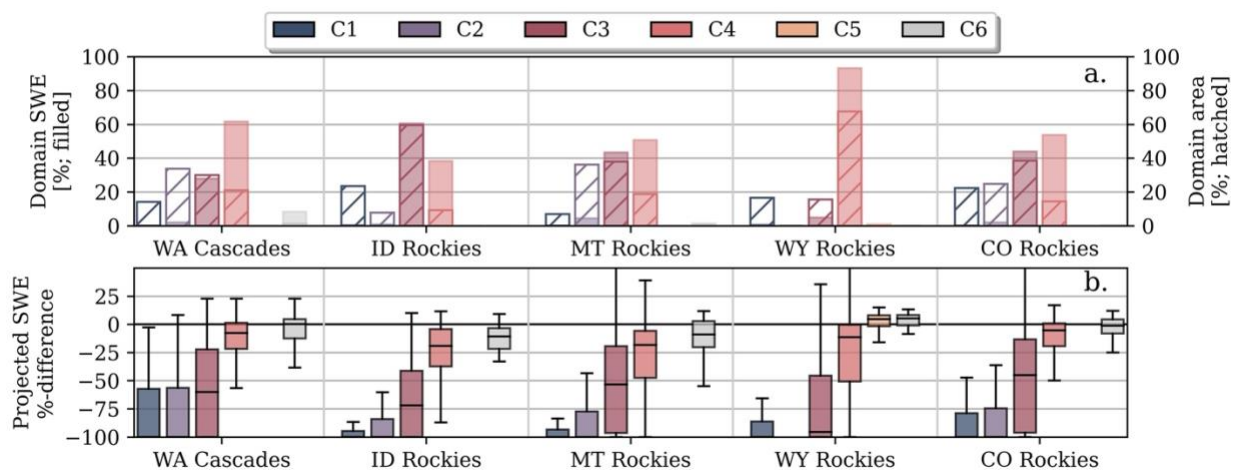
504 Repeating the classifications from above in other domains (Figure S2 – S10), we could see
505 that the snow classes appeared in each domain, but were shifted in elevation (Figure 7). For
506 example, the snow classes in the nearby ID Rockies domain spanned elevation bands that were
507 almost identical to those from the WA Cascades domain discussed above. However, the location
508 of these snow classes was shifted up in elevation by approximately 400 m in the MT Rockies,
509 750 m in the WY Rockies, and 1550 m in the CO Rockies. Relative to 15 April, the 15 May
510 snow line advanced up in elevation as snow extents were reduced from spring snowmelt in each
511 domain, causing a growth in the elevations representing the first three snow classes (C1, C2, and
512 C3), and a reduction to the elevations where the difference between snow projections exceeded
513 the difference in SWE distributions between the early 21st century and end-of-century periods
514 (C4) (Figure 7).



515
 516 Figure 7. The elevations (x-axis) spanned by each snow class within each domain (y-axis) on 15
 517 April (hollow) and 15 May (hatched).

518 Of the five domains investigated here, the SWE climate change signals in the WY Rockies
 519 domain were the most unique (Figure 1, Figure S7, Figure S8, and Table 1). Notably, 15 April
 520 model disparities exceeded the SWE change signal (C4) for grid cells between approximately
 521 2050 – 3550 m elevation, a span of elevations approximately 2.5 times larger than the C4 snow
 522 class in the other domains (Figure 7). This was likely driven by the winter climate in the interior
 523 WY Rockies, which was the coldest domain simulated here, and thereby had the smallest
 524 projected changes to 15 April end-of-century SWE on 15 April (Figure S7). However, the
 525 DBCCA6 data projected decreases to 15 April SWE that were as high as 52% across mid and
 526 high elevation grid cells (Figure 3). This is discussed more in Section 5. Despite the outlying
 527 projections from the DBCCA6 dataset, the WY Rockies domain was also the only domain to
 528 project SWE *increases* that were larger, on average, than the disparity across the models (Figure
 529 7, C5). These grid cells were concentrated at elevations of 3550 – 3750m, although ensemble-
 530 median increases to 15 April SWE occurred at elevations as low as 2450 m for the NEX6-M
 531 projection dataset.

532 On 15 April, more than 90% of each domain's snow volume (e.g., Figure 5d) fell within
 533 classes where either the size of projected SWE decreases exceeded model disparities (C3) or
 534 model disparities exceeded projected changes to SWE (C4) (Figure 8a). Across the five domains,
 535 only in the ID Rockies domain did a majority (59%) of the domain's 15 April historical snow
 536 volume fall in regions where model disparities were smaller than the SWE climate change signal
 537 (C3). Despite containing a large portion of each domain's snow volume, the C4 snow class
 538 covered relatively small areal extents, covering only 22%, 9%, 10%, and 18% of the WA
 539 Cascades, ID Rockies, MT Rockies, and CO Rockies domains, respectively. As noted above,
 540 projections in the WY Rockies domain behaved differently, with 66% of the domain area and
 541 93% of the domain's SWE volume exhibiting model disparities that were greater than the climate
 542 change signal. The proportion of the area and SWE volume that fell within each snow class on
 543 15 April were largely flipped on 15 May (Figure S11), with a majority of snow volume (58 –
 544 94%) existing in elevations where the climate change signal exceeded the model disparity.
 545 Again, the WY Rockies domain exhibited different patterns with 40% of the snow volume
 546 existing in the C3 class, and 58% existing in the C4 class, despite the C4 class only covering
 547 approximately 18% of the domain area.



548

549 Figure 8. Bars show a) 15 April domain area (hatched) and SWE volume (filled) within each of
550 the snow classes in each domain (x-axis). b) boxplots depict the distribution of all projected
551 changes to 15 April SWE in each domain and snow class.

552 **5. Discussion**

553 The results in Section 4 compared 124 snow projections, including climate projections from
554 two CMIP phases (CMIP5 and CMIP6), 58 GCMs, and six modeling approaches employing
555 different downscaling approaches, downscaling reference datasets, spatial resolutions, and land
556 surface models. Despite these differences, the snow projection datasets exhibited relationships
557 with one another that had consistencies across each of the domains. For example, NEX6-M and
558 NEX6-C snow projections had large changes in end-of-century SWE projections (approximately
559 -13% per every 100 m decrease in elevation, on average) across 300 – 600 m spans in elevation.
560 While this study does not investigate or attribute the sources of differences between snow
561 projections, we hypothesize these sharp gradients in the SWE percent change signals were driven
562 by the delta-method approach used by the NEX6-M and NEX6-C projections, which applied the
563 same spatial maps of monthly climate-change perturbations (Section 2.2), resulting in climate
564 impacts on SWE projections that were far more localized in space than the other projection
565 datasets. Despite this, NEX6-C projected larger decreases to end-of-century SWE than NEX6-M
566 projections in each domain. This was driven by the low snow years (e.g., water years 1998, 2001,
567 2004, 2005, and 2009 in the WA Cascades) which had shallower low-elevation snow on 15
568 April, and increased sensitivity to increases in air temperature and melt energy.

569 SWE projections from the DBCCA6 dataset estimated significantly larger decreases to end-of-
570 century 15 April SWE in each domain. This was particularly the case in the WY Rockies
571 domain, where median SWE decreases exceeded 50% across all elevations, but a majority of the
572 domain's snow volume resided in elevations where other snow projections estimated little-to-no
573 change (-10% to +10%) (Figure S7). These outlying projections may have been driven by the

574 downscaling procedure using the Daymet meteorological dataset (Thornton et al., 2021), which
575 is relatively warmer than other reference meteorological datasets (Oyler et al., 2015). The
576 DBCCA6 dataset also projected earlier dates of peak SWE, resulting in larger proportions of
577 SWE melt prior to 15 April than the other projection datasets (Figure S12).

578 The relationship between elevation and 15 April projected changes to SWE were propagated
579 into the 15 May snow projections in each domain and projection dataset (Figure 6). In fact, the
580 elevational pattern of 15 May projected changes to SWE could be reconstructed by 1) shifting
581 the 15 April SWE projections up in elevation, and 2) adding increases to spring snowmelt, which
582 were larger at lower elevations, but decreased with elevation. On average, across the five
583 domains, the spatial Pearson Correlation Coefficient between 15 April and 15 May SWE
584 projections (Figure 6) was 0.82 for the NEX6-M projections (on average, across the 5 domains),
585 0.96 for the NEX6-C projections, 0.92 for the LOCA5 projections, 0.96 for the BCSD5
586 projections, 0.97 for the MACA5 projections, and 0.88 for the DBCCA6 projections. As
587 discussed in Section 4.1, the slope of the relationship between the 15 April and 15 May SWE
588 projections was most influenced by the elevational pattern of 15 April SWE projections. For
589 example, 15 April SWE projections in the WY Rockies domain exhibited sharper gradients with
590 elevation (Figure S7). When this SWE projection pattern was shifted up in elevation on 15 May
591 (Figure S8), many grid cells with little-to-no 15 April SWE losses exhibited losses of 25% or
592 greater on 15 May, causing a more dramatic slope in the relationship between 15 April and 15
593 May SWE projections in this domain, relative to other domains (Figure 6).

594 The consistent patterns between the different snow projections, and the hysteresis in these
595 patterns over time, suggested that the coherent relationships between the snow projections can be
596 used to identify classes where and when 1) disparate approaches converge to common

597 projections of future change, and 2) improvements in systematic projection disparities could
598 provide the greatest improvement in projections of future snow water resources. In Section 4, we
599 chose to classify these snow classes using the NOS statistic (Equation 3), which benchmarked
600 the disparities across snow projection datasets versus the underlying climate change signals. To
601 our knowledge, this type of approach has not been used in other studies. However, we found that
602 the NOS statistic had multiple benefits. First, this approach relied on U -values from the Mann-
603 Whitney non-parametric ranked sum test, which standardized the overlap between two datasets
604 by the number of samples in each (Equations 1 and 2, n_1 and n_2). Relative to more common
605 measurements (e.g., percentiles of overlap and ANOVA analyses) NOS provided a continuous
606 normalized statistic ranging between 0.0 and 0.5 that was less-sensitive to comparisons between
607 projections with different numbers of GCMs. Additionally, SWE projections across 100 m
608 elevation bands did not consistently conform to any theoretical distribution (e.g, normal,
609 lognormal, chi, etc.), indicating that a statistic based on a non-parametric test, such as the Mann-
610 Whitney U, would perform best.

611 Much like the projected changes to end-of-century SWE, the distribution of the NOS statistic
612 for 15 April climate change signals (Figure 2a) and model disparities (Figure 2b) followed
613 similar patterns with increases in elevation across the modeling domains (Figure 5c, Figure S3c,
614 Figure S5c, Figure S7c, Figure S9c). This resulted in the similar, but elevation-shifted
615 distribution of snow classes (C1 – C6) shown in Figure 7. Overall, the climate change signal
616 varied with elevation more than the projection disparity. For example, in the WA Cascades
617 domain on 15 April (Figure 5c), the standard deviation of the NOS statistic for the climate
618 change signal was 49% larger than the standard deviation of the NOS for model disparities. In
619 this same domain, the distributions of NOS for the climate change and model disparity signals

620 were approximately equal at an elevation of 1550 m (Figure 5c). This inflection point
621 represented the location where snow losses projected at lower elevations (C1 – C3, 250 – 1550
622 m) were in agreement in sign (positive/negative) and of similar magnitudes, but the disparity
623 across models exceeded the climate change signal at higher elevations (C4). For the 124 snow
624 projections tested here, the median projected change to 15 April SWE at this inflection point was
625 approximately -26% in the WA Cascades (Figure 8). For the other domains, these inflection
626 points occurred at: 1650 m elevation and -48% projected changes to SWE in the ID Rockies,
627 1950 m and -44% in the MT Rockies, 2250 m and -35% in the WY Rockies, and 2750 m and -
628 23% in the CO Rockies.

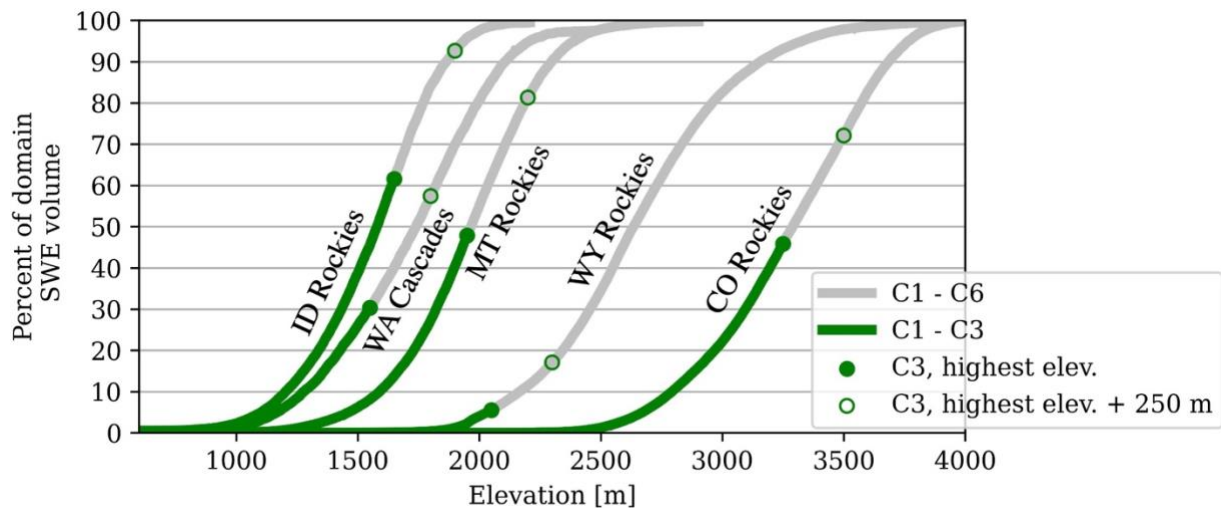
629 Based on the inflection points above, grid cells with 15 April ensemble-average projected
630 decreases to SWE of 48% or greater (Figure 3) were among the highest-confidence climate
631 change signals. Siirila-Woodburn et al. (2021) suggested that end-of-winter projected SWE
632 losses of 48% or greater are likely for the vast majority of Western US by the end of the century.
633 However, disproportionate amounts of annual Western US streamflow come from high-elevation
634 montane regions which cover only small portions of the Western US land mass (Li et al., 2017),
635 and are subject to some of the highest snow projection uncertainties. In this study, Figure 8a
636 shows that snow classes with higher-confidence projected SWE decreases (snow classes C1 –
637 C3) account for more than half of the area of the WA Cascades, ID Rockies, MT Rockies, and
638 CO Rockies domains. Yet, these areas contain less than 63%, and as little as 6%, of each
639 domain's historical snow volume. In other words, while projections employing disparate
640 modeling approaches agree across large spatial extents, the locations with disagreements contain
641 disproportionate amounts of snow. This issue was particularly prevalent in the WY Rockies

642 domain where only 5% and 1% of the historical snow volume had higher-confidence SWE
643 decreases (C1 – C3) and SWE increases (C5), respectively.

644 We found that 15 April model disparity measured using the NOS statistic (Figure 2b) was at
645 it's worst for elevations approximately 250 m higher than the inflection points. In these
646 elevations, SWE projections from the NEX6-M and NEX6-C SWE datasets tended to diverge
647 from the LOCA5, BCSD5, and MACA5 projections, approaching smaller end-of-century SWE
648 change estimates. This was opposed to SWE projections for the DBCCA6 dataset, which
649 estimated larger SWE losses than any other dataset for elevations both in this span of elevations,
650 and at all higher elevations. Although limited in area, this 250 m elevation band contained
651 significant amounts of SWE volume (Figure 9), accounting for 27% of the historical snow
652 volume in the WA Cascades, 31% in the ID Rockies, 33% in the MT Rockies, 11% in the WY
653 Rockies, and 26% in the CO Rockies.

654 Based on Figure 9, and the snow projection datasets compared in this study, we expect that the
655 greatest improvements to the coherence of snow projections could come from investigating and
656 attributing the sources of projection disparities in the 250 m elevation bands above the inflection
657 points. However, we recognize that improving the coherence of snow projections in these
658 regions is challenging. For example, for the domains investigated here, the average terrain slope
659 in the 250 m elevation bands above the inflection point is approximately 14°. This means that for
660 a conservative and steadily-increasing slope, elevation increases approximately 249 m for every
661 1000 m in horizontal distance. Assuming common air temperature lapse rates (e.g., Arsenault et
662 al., 2018; Minder et al., 2010), air temperature within a 100 km GCM grid cell with these
663 characteristics vary consistently by as much as 8° C, and often more. This highlights the
664 challenges with modeling meteorological conditions at at scales significantly smaller than the

665 spatial resolutions of GCMs, especially considering fine-scale processes like mountain pass air
 666 mixing and snow albedo feedbacks. Grid cells within these 250 m elevation bands are also often
 667 in inaccessible, hazardous, and unmonitored terrain. In fact, the 250 m elevation band of focus in
 668 the CO Rockies domain falls at approximately 3250 – 3500 m in elevation, which is higher than
 669 approximately 95% of Snow Telemetry (SNOTEL) stations in the Western United States,
 670 making it difficult to validate GCMs and reference downscaling datasets. Fortunately, since
 671 disparities across snow projections demonstrated repeatable, but elevation-shifted patterns in
 672 each domain, we hypothesize that improvements to projection disparities in one domain may
 673 translate to improvements in other domains. In other words, while the cause of disparities
 674 between models may be difficult to diagnose in this high elevation region in the CO Rockies, the
 675 pattern of disparities between projections in this regions was similar to the pattern of disparities
 676 at more-accessible and observed elevations between 1550 and 1800 m in the WA Cascades. This
 677 hypothesis is beyond the scope of this manuscript, and will be investigated by future research.



678
 679 Figure 9. Historical SWE distribution in each domain for all snow classes (gray), and snow
 680 classes with the most-coherent decreases to end-of-century SWE (green). The difference between
 681 the filled and hollow scatter points show the difference in SWE volume over a 250 m elevation
 682 band above the elevation at which model disparity first equals the climate change signal.

683 Our results show that benchmarking ensembles of snow projection climate change signals
684 using the disparity across models can provide a path forward for identifying coherence between
685 projections, both in terms of identifying locations where disparate modeling methodologies
686 approach common results, and identifying systematic and repeatable departures between snow
687 projection datasets. We acknowledge that the results presented here were dependent on the six
688 snow projections used, and the two analogous emissions scenarios (SSP 2-4.5 and RCP 4.5).
689 Therefore, future research should continue on this approach, adding more snow projections
690 including a range of climate forcing and modeling approaches. Given the continued development
691 of state-of-the-art climate models, meteorological downscaling approaches, and land surface
692 models, we expect large-ensemble approaches like the approaches used here to be valuable for
693 identifying and communicating the high-confidence changes to future snow water resources and
694 the resulting impacts on the land surface hydrology, and identifying the regions where our
695 estimates of future snowpack may benefit most from further research and development.

696 **6. Conclusions**

697 Differences in modeling approaches such as different land surface models, climate models,
698 downscaling approaches, and spatial resolutions can cause cascading differences in model
699 forcing and simulated snow evolution, making it difficult to determine the most accurate
700 projections, and the causes of disparities between different projection datasets. This is
701 particularly the case in mountainous terrain, where the sparsity of observations and fine-scale
702 spatial variabilities in meteorological conditions make climate and snow projections challenging.

703 Here, we found that projected changes to end-of-century SWE, climate change signals, and
704 model disparities showed relationships with terrain elevation in five Western US montane
705 domains. Using these relationships, we were able to partition each domain into snow classes that

706 exhibited similar relationships, but were shifted in elevation (Figure 7). The lowest elevations of
707 each domain exhibited high-confidence projected decreases to 15 April SWE that were larger in
708 magnitude than the disparity across the models (Figure 3 and Figure 5). Across the five domains,
709 15 April projections agreed in regions where median projected decreases to end-of-century SWE
710 were 48% or larger. However, some regions like the Colorado Rockies and Washington
711 Cascades had better coherence across the projections, resulting in decreases to end-of-century
712 SWE with high levels of agreement between snow projections at grid cells experiencing more
713 than 23% and 26% decreases, respectively. Grid cells with high-confidence SWE projections
714 covered a majority of the domain area in the Washington Cascades, Idaho Rockies, Montana
715 Rockies, and Colorado Rockies (Figure 8). Despite this, a majority of annual SWE volume
716 existed in higher elevation regions where the disparities between snow projections exceeded the
717 projected changes to SWE. This was particularly the case in the Wyoming Rockies domain,
718 where colder climates resulted in significantly smaller projected changes to 15 April SWE
719 (Figure 3). In fact, only this domain experienced grid cells with projected high-confidence
720 *increases* to end-of-century SWE. However, this only occurred over a small span of elevations
721 (3550 – 3750 m), accounting for approximately 1% of this domain’s total area, and less than 1%
722 of the total SWE volume. In summary, we found that despite the widespread agreement in snow
723 projections spatially, the greatest disagreements between projections occurred in the regions with
724 the greatest snow volumes, emphasizing the need to improve snow projection coherence in high-
725 elevation terrain.

726 Results also found strong relationships ($r \geq 0.82$) between 15 April and 15 May SWE
727 projections for each snow projection dataset in each domain (Figure 6). In fact, 15 May SWE
728 projections could be reproduced by shifting the 15 April SWE projections up in elevation, and

729 enhancing the snowmelt that occurred for thinner snowpacks in warmer future climates. This
730 suggested that improvements to the spread and certainty of 15 April SWE projections would
731 translate to improvements between the projections at later dates. These results suggest that future
732 studies should consider the use of large-ensemble approaches, like the approach used here, with
733 additional snow projection datasets and future emissions scenarios, as a basis for 1) identifying
734 and communicating the highest-confidence changes to future snow water resources, and 2) the
735 locations and periods where work should focus most on honing future projection datasets.

736 **Acknowledgements**

737 This work was supported in part by funding from the National Aeronautics and Space
738 Administration (NASA) Terrestrial Hydrology Program. Computing was supported by the
739 NASA Center for Climate Simulation (NCCS) and the Oak Ridge Leadership Computing
740 Facility at Oak Ridge National Laboratory, which is a Department of Energy Office of Science
741 User Facility. The authors would also like to acknowledge support from the US Geological
742 Survey (grant no. G21AC10645), in addition to insight and advice provided by the US Fish and
743 Wildlife Service and Dr. Stefan Rahimi. The authors declare that they have no conflict of
744 interest.

745 **Data Availability Statement**

746 The Western United States SWE reanalysis can be accessed through the National Snow and Ice
747 Data Center (Fang and Margulis, 2020). BCSD5 and LOCA5 (Table 1) projections can be
748 accessed from Maurer et al. (2007). MACA5 data can be accessed from the Northwest
749 Knowledge Network (Abatzoglou et al., 2014). DBCCA6 projections can be accessed from Kao
750 et al. (2022b). Finally, the novel dataset generated for this project can be accessed through the
751 NASA NCCS data portal, this includes the NEX-GDDP-CMIP6 climate forcing

752 (<https://ds.nccs.nasa.gov/thredds/catalog/AMES/NEX/GDDP-CMIP6/catalog.html>), and the
753 NEX6-M and NEX-C snow simulation outputs (https://portal.nccs.nasa.gov/lisdata_pub/FWS/).
754 The authors are actively working on providing the NEX6-M and NEX6-C snow projections to
755 persistent and doi-citable data repositories.

756 **References**

- 757 Aas, K.S., Gislén, K., Westermann, S., Berntsen, T.K., 2017. A Tiling Approach to Represent
758 Subgrid Snow Variability in Coupled Land Surface–Atmosphere Models. *J.*
759 *Hydrometeor.* 18, 49–63. <https://doi.org/10.1175/JHM-D-16-0026.1>
- 760 Abatzoglou, J., Hegewisch, K., Hegewisch, K., Hegewisch, K., 2014. MACAv2-LIVNEH:
761 Gridded Daily Statistical Downscaling of CMIP5 using LIVNEH training dataset. USGS
762 ScienceBase.
- 763 Abatzoglou, J.T., Brown, T.J., 2012. A comparison of statistical downscaling methods suited for
764 wildfire applications. *International Journal of Climatology* 32, 772–780.
765 <https://doi.org/10.1002/joc.2312>
- 766 Alder, J.R., Hostetler, S.W., 2019. The Dependence of Hydroclimate Projections in Snow-
767 Dominated Regions of the Western United States on the Choice of Statistically
768 Downscaled Climate Data. *Water Resources Research* 55, 2279–2300.
769 <https://doi.org/10.1029/2018WR023458>
- 770 Arsenault, K.R., Kumar, S.V., Geiger, J.V., Wang, S., Kemp, E., Mocko, D.M., Beaudoin,
771 H.K., Getirana, A., Navari, M., Li, B., Jacob, J., Wegiel, J., Peters-Lidard, C.D., 2018.
772 The Land surface Data Toolkit (LDT v7.2) – a data fusion environment for land data
773 assimilation systems. *Geoscientific Model Development* 11, 3605–3621.
774 <https://doi.org/10.5194/gmd-11-3605-2018>
- 775 Barnett, T.P., Adam, J.C., Lettenmaier, D.P., 2005. Potential impacts of a warming climate on
776 water availability in snow-dominated regions. *Nature* 438, 303.
777 <https://doi.org/10.1038/nature04141>
- 778 Barsugli, J.J., Ray, A.J., Livneh, B., Dewes, C.F., Heldmyer, A., Rangwala, I., Guinotte, J.M.,
779 Torbit, S., 2020. Projections of Mountain Snowpack Loss for Wolverine Denning
780 Elevations in the Rocky Mountains. *Earth’s Future* 8, e2020EF001537.
781 <https://doi.org/10.1029/2020EF001537>
- 782 Brekke, L., Thrasher, B.L., Maurer, E.P., Pruitt, T., 2013. Downscaled CMIP3 and CMIP5
783 Climate and Hydrology Projections: Release of Downscaled CMIP5 Climate Projections,
784 Comparison with Preceding Information, and Summary of User Needs. US Bureau of
785 Reclamation.
- 786 Chegwidan, O.S., Nijssen, B., Rupp, D.E., Arnold, J.R., Clark, M.P., Hamman, J.J., Kao, S.-C.,
787 Mao, Y., Mizukami, N., Mote, P.W., Pan, M., Pytlak, E., Xiao, M., 2019. How Do
788 Modeling Decisions Affect the Spread Among Hydrologic Climate Change Projections?
789 Exploring a Large Ensemble of Simulations Across a Diversity of Hydroclimates. *Earth’s*
790 *Future* 7, 623–637. <https://doi.org/10.1029/2018EF001047>
- 791 Clark, M.P., Hendrikx, J., Slater, A.G., Kavetski, D., Anderson, B., Cullen, N.J., Kerr, T.,
792 Hreinsson, E.Ö., Woods, R.A., 2011. Representing spatial variability of snow water

793 equivalent in hydrologic and land-surface models: A review. *Water Resources Research*
794 47. <https://doi.org/10.1029/2011WR010745>

795 Currier, W.R., Thorson, T., Lundquist, J.D., 2017. Independent Evaluation of Frozen
796 Precipitation from WRF and PRISM in the Olympic Mountains. *J. Hydrometeor.* 18,
797 2681–2703. <https://doi.org/10.1175/JHM-D-17-0026.1>

798 Essery, R., Morin, S., Lejeune, Y., B Ménard, C., 2013. A comparison of 1701 snow models
799 using observations from an alpine site. *Advances in Water Resources, Snow–Atmosphere*
800 *Interactions and Hydrological Consequences* 55, 131–148.
801 <https://doi.org/10.1016/j.advwatres.2012.07.013>

802 Eyring, V., Bony, S., Meehl, G.A., Senior, C.A., Stevens, B., Stouffer, R.J., Taylor, K.E., 2016.
803 Overview of the Coupled Model Intercomparison Project Phase 6 (CMIP6) experimental
804 design and organization. *Geoscientific Model Development* 9, 1937–1958.
805 <https://doi.org/10.5194/gmd-9-1937-2016>

806 Fang, Y., Liu, Y., Margulis, S.A., 2022. A western United States snow reanalysis dataset over
807 the Landsat era from water years 1985 to 2021. *Sci Data* 9, 677.
808 <https://doi.org/10.1038/s41597-022-01768-7>

809 Fang, Y., Liu, Y., Margulis, S.A., 2020. A New Landsat-era Snow Reanalysis Dataset over the
810 Western United States 2020, C047-0017.

811 Fang, Y., Margulis, S.A., 2020. Western United States UCLA Daily Snow Reanalysis, Version 1
812 [WWW Document]. National Snow and Ice Data Center Distributed Active Archive
813 Center. URL <https://doi.org/10.5067/PP7T2GBI52I2> (accessed 7.28.23).

814 Fyfe, J.C., Derksen, C., Mudryk, L., Flato, G.M., Santer, B.D., Swart, N.C., Molotch, N.P.,
815 Zhang, X., Wan, H., Arora, V.K., Scinocca, J., Jiao, Y., 2017. Large near-term projected
816 snowpack loss over the western United States. *Nat Commun* 8, 14996.
817 <https://doi.org/10.1038/ncomms14996>

818 Gelaro, R., McCarty, W., Suárez, M.J., Todling, R., Molod, A., Takacs, L., Randles, C.A.,
819 Darmenov, A., Bosilovich, M.G., Reichle, R., Wargan, K., Coy, L., Cullather, R., Draper,
820 C., Akella, S., Buchard, V., Conaty, A., Silva, A.M. da, Gu, W., Kim, G.-K., Koster, R.,
821 Lucchesi, R., Merkova, D., Nielsen, J.E., Partyka, G., Pawson, S., Putman, W.,
822 Rienecker, M., Schubert, S.D., Sienkiewicz, M., Zhao, B., 2017. The Modern-Era
823 Retrospective Analysis for Research and Applications, Version 2 (MERRA-2). *Journal of*
824 *Climate* 30, 5419–5454. <https://doi.org/10.1175/JCLI-D-16-0758.1>

825 Gergel, D.R., Nijssen, B., Abatzoglou, J.T., Lettenmaier, D.P., Stumbaugh, M.R., 2017. Effects
826 of climate change on snowpack and fire potential in the western USA. *Climatic Change*
827 141, 287–299.

828 Ghan, S.J., Shippert, T., 2006. Physically Based Global Downscaling: Climate Change
829 Projections for a Full Century. *Journal of Climate* 19, 1589–1604.
830 <https://doi.org/10.1175/JCLI3701.1>

831 Guan, B., Waliser, D.E., Ralph, F.M., Fetzer, E.J., Neiman, P.J., 2016. Hydrometeorological
832 characteristics of rain-on-snow events associated with atmospheric rivers. *Geophysical*
833 *Research Letters* 43, 2964–2973. <https://doi.org/10.1002/2016GL067978>

834 Gutmann, E., Pruitt, T., Clark, M.P., Brekke, L., Arnold, J.R., Raff, D.A., Rasmussen, R.M.,
835 2014. An intercomparison of statistical downscaling methods used for water resource
836 assessments in the United States. *Water Resources Research* 50, 7167–7186.
837 <https://doi.org/10.1002/2014WR015559>

838 Gutmann, E.D., Rasmussen, R.M., Liu, C., Ikeda, K., Gochis, D.J., Clark, M.P., Dudhia, J.,
839 Thompson, G., 2012. A Comparison of Statistical and Dynamical Downscaling of Winter
840 Precipitation over Complex Terrain. *J. Climate* 25, 262–281.
841 <https://doi.org/10.1175/2011JCLI4109.1>

842 Hale, K.E., Wlostowski, A.N., Badger, A.M., Musselman, K.N., Livneh, B., Molotch, N.P.,
843 2022. Modeling streamflow sensitivity to climate warming and surface water inputs in a
844 montane catchment. *Journal of Hydrology: Regional Studies* 39, 100976.
845 <https://doi.org/10.1016/j.ejrh.2021.100976>

846 Hamlet, A.F., Mote, P.W., Clark, M.P., Lettenmaier, D.P., 2007. Twentieth-Century Trends in
847 Runoff, Evapotranspiration, and Soil Moisture in the Western United States*. *Journal of*
848 *Climate* 20, 1468–1486. <https://doi.org/10.1175/JCLI4051.1>

849 Harpold, A., Brooks, P., Rajagopal, S., Heidebuchel, I., Jardine, A., Stielstra, C., 2012. Changes
850 in snowpack accumulation and ablation in the intermountain west. *Water Resources*
851 *Research* 48. <https://doi.org/10.1029/2012WR011949>

852 Harpold, A.A., Brooks, P.D., 2018. Humidity determines snowpack ablation under a warming
853 climate. *Proceedings of the National Academy of Sciences* 115, 1215–1220.
854 <https://doi.org/10.1073/pnas.1716789115>

855 Hawkins, E., Sutton, R., 2009. The Potential to Narrow Uncertainty in Regional Climate
856 Predictions. *Bulletin of the American Meteorological Society* 90, 1095–1108.
857 <https://doi.org/10.1175/2009BAMS2607.1>

858 Hidalgo, H.G., Dettinger, M.D., Cayan, D.R., 2008. Downscaling with constructed analogues:
859 Daily precipitation and temperature fields over the United States. California Energy
860 Commission PIER Final Project Report CEC-500-2007-123.

861 Hughes, M., Hall, A., Fovell, R.G., 2009. Blocking in Areas of Complex Topography, and Its
862 Influence on Rainfall Distribution. *Journal of the Atmospheric Sciences* 66, 508–518.
863 <https://doi.org/10.1175/2008JAS2689.1>

864 Hughes, M., Lundquist, J.D., Henn, B., 2017. Dynamical downscaling improves upon gridded
865 precipitation products in the Sierra Nevada, California. *Clim Dyn.*
866 <https://doi.org/10.1007/s00382-017-3631-z>

867 Ikeda, K., Rasmussen, R., Liu, C., Newman, A., Chen, F., Barlage, M., Gutmann, E., Dudhia, J.,
868 Dai, A., Luce, C., Musselman, K., 2021. Snowfall and snowpack in the Western U.S. as
869 captured by convection permitting climate simulations: current climate and pseudo global
870 warming future climate. *Clim Dyn* 57, 2191–2215. <https://doi.org/10.1007/s00382-021-05805-w>

871

872 IPCC, 2021. Climate change 2021: The physical science basis. Contribution of Working Group I
873 to the sixth assessment report of the Intergovernmental Panel on Climate Change
874 [Masson-Delmotte, V., P. Zhai, A. Pirani, S.L. Connors, C. Péan, S. Berger, N. Caud, Y.
875 Chen, L. Goldfarb, M.I. Gomis, M. Huang, K. Leitzell, E. Lonnoy, J.B.R. Matthews,
876 T.K. Maycock, T. Waterfield, O. Yelekçi, R. Yu, and B. Zhou (eds.)]. Cambridge
877 University Press, Cambridge, U.K., and New York, NY, USA.

878 Jennings, K.S., Winchell, T.S., Livneh, B., Molotch, N.P., 2018. Spatial variation of the rain–
879 snow temperature threshold across the Northern Hemisphere. *Nat Commun* 9, 1148.
880 <https://doi.org/10.1038/s41467-018-03629-7>

881 Kao, S.-C., Ashfaq, M., Rastogi, D., Gangrade, S., Uria Martinez, R., Fernandez, A., Konapala,
882 G., Voisin, N., Zhou, T., Xu, W., Gao, H., Zhao, B., Zhao, G., 2022a. The Third
883 Assessment of the Effects of Climate Change on Federal Hydropower (No. ORNL/TM-

884 2021/2278). Oak Ridge National Lab. (ORNL), Oak Ridge, TN (United States).
885 <https://doi.org/10.2172/1887712>

886 Kao, S.-C., Moetasim, A., Deeksha, R., Gangrade, S., 2022b. CMIP6-based Multi-model
887 Hydroclimate Projection over the Conterminous US. HydroSource.
888 <https://doi.org/10.21951/SWA9505V3/1887469>

889 Kapnick, S., Hall, A., 2012. Causes of recent changes in western North American snowpack.
890 *Clim Dyn* 38, 1885–1899. <https://doi.org/10.1007/s00382-011-1089-y>

891 Kim, R.S., Kumar, S., Vuyovich, C., Houser, P., Lundquist, J., Mudryk, L., Durand, M., Barros,
892 A., Kim, E.J., Forman, B.A., Gutmann, E.D., Wrzesien, M.L., Garnaud, C., Sandells, M.,
893 Marshall, H.-P., Cristea, N., Pflug, J.M., Johnston, J., Cao, Y., Mocko, D., Wang, S.,
894 2021. Snow Ensemble Uncertainty Project (SEUP): quantification of snow water
895 equivalent uncertainty across North America via ensemble land surface modeling. *The*
896 *Cryosphere* 15, 771–791. <https://doi.org/10.5194/tc-15-771-2021>

897 Koster, R.D., Mahanama, S.P.P., Livneh, B., Lettenmaier, D.P., Reichle, R.H., 2010. Skill in
898 streamflow forecasts derived from large-scale estimates of soil moisture and snow.
899 *Nature Geosci* 3, 613–616. <https://doi.org/10.1038/ngeo944>

900 Krinner, G., Derksen, C., Essery, R., Flanner, M., Hagemann, S., Clark, M., Hall, A., Rott, H.,
901 Brutel-Vuilmet, C., Kim, H., Ménard, C.B., Mudryk, L., Thackeray, C., Wang, L.,
902 Arduini, G., Balsamo, G., Bartlett, P., Boike, J., Boone, A., Chéruy, F., Colin, J., Cuntz,
903 M., Dai, Y., Decharme, B., Derry, J., Ducharne, A., Dutra, E., Fang, X., Fierz, C.,
904 Ghattas, J., Gusev, Y., Haverd, V., Kontu, A., Lafaysse, M., Law, R., Lawrence, D., Li,
905 W., Marke, T., Marks, D., Ménégoz, M., Nasonova, O., Nitta, T., Niwano, M., Pomeroy,
906 J., Raleigh, M.S., Schaedler, G., Semenov, V., Smirnova, T.G., Stacke, T., Strasser, U.,
907 Svenson, S., Turkov, D., Wang, T., Wever, N., Yuan, H., Zhou, W., Zhu, D., 2018. ESM-
908 SnowMIP: assessing snow models and quantifying snow-related climate feedbacks.
909 *Geoscientific Model Development* 11, 5027–5049. [https://doi.org/10.5194/gmd-11-5027-](https://doi.org/10.5194/gmd-11-5027-2018)
910 2018

911 Le Roux, R., Katurji, M., Zawar-Reza, P., Quénol, H., Sturman, A., 2018. Comparison of
912 statistical and dynamical downscaling results from the WRF model. *Environmental*
913 *Modelling & Software* 100, 67–73. <https://doi.org/10.1016/j.envsoft.2017.11.002>

914 Lehner, F., Deser, C., Maher, N., Marotzke, J., Fischer, E.M., Brunner, L., Knutti, R., Hawkins,
915 E., 2020. Partitioning climate projection uncertainty with multiple large ensembles and
916 CMIP5/6. *Earth System Dynamics* 11, 491–508. <https://doi.org/10.5194/esd-11-491-2020>

917 Leung, L.R., Qian, Y., Bian, X., Washington, W.M., Han, J., Roads, J.O., 2004. Mid-Century
918 Ensemble Regional Climate Change Scenarios for the Western United States. *Climatic*
919 *Change* 62, 75–113. <https://doi.org/10.1023/B:CLIM.0000013692.50640.55>

920 Li, D., Wrzesien, M.L., Durand, M., Adam, J., Lettenmaier, D.P., 2017. How much runoff
921 originates as snow in the western United States, and how will that change in the future?
922 *Geophysical Research Letters* 44, 6163–6172. <https://doi.org/10.1002/2017GL073551>

923 López-Moreno, J.I., Gascoin, S., Herrero, J., Sproles, E.A., Pons, M., Alonso-González, E.,
924 Hanich, L., Boudhar, A., Musselman, K.N., Molotch, N.P., Sickman, J., Pomeroy, J.,
925 2017. Different sensitivities of snowpacks to warming in Mediterranean climate
926 mountain areas. *Environ. Res. Lett.* 12, 074006. [https://doi.org/10.1088/1748-](https://doi.org/10.1088/1748-9326/aa70cb)
927 9326/aa70cb

928 Lumbrazo, C., Bennett, A., Currier, W.R., Nijssen, B., Lundquist, J., 2022. Evaluating Multiple
929 Canopy-Snow Unloading Parameterizations in SUMMA With Time-Lapse Photography

930 Characterized by Citizen Scientists. *Water Resources Research* 58, e2021WR030852.
931 <https://doi.org/10.1029/2021WR030852>

932 Lundquist, J.D., Hughes, M., Henn, B., Gutmann, E.D., Livneh, B., Dozier, J., Neiman, P., 2015.
933 High-Elevation Precipitation Patterns: Using Snow Measurements to Assess Daily
934 Gridded Datasets across the Sierra Nevada, California. *J. Hydrometeorol.* 16, 1773–1792.
935 <https://doi.org/10.1175/JHM-D-15-0019.1>

936 Lundquist, J.D., Minder, J.R., Neiman, P.J., Sukovich, E., 2010. Relationships between Barrier
937 Jet Heights, Orographic Precipitation Gradients, and Streamflow in the Northern Sierra
938 Nevada. *Journal of Hydrometeorology* 11, 1141–1156.
939 <https://doi.org/10.1175/2010JHM1264.1>

940 Maurer, E.P., Brekke, L., Pruitt, T., Duffy, P.B., 2007. Fine-resolution climate change
941 projections enhance regional climate change impact studies. *Eos, Transactions, American*
942 *Geophysical Union* 88, 504. <https://doi.org/doi:10.1029/2007EO470006>

943 McCrary, R.R., Mearns, L.O., 2019. Quantifying and Diagnosing Sources of Uncertainty in
944 Midcentury Changes in North American Snowpack from NARCCAP. *Journal of*
945 *Hydrometeorology* 20, 2229–2252. <https://doi.org/10.1175/JHM-D-18-0248.1>

946 Minder, J.R., Letcher, T.W., Skiles, S.M., 2016. An evaluation of high-resolution regional
947 climate model simulations of snow cover and albedo over the Rocky Mountains, with
948 implications for the simulated snow-albedo feedback. *Journal of Geophysical Research:*
949 *Atmospheres* 121, 9069–9088. <https://doi.org/10.1002/2016JD024995>

950 Minder, J.R., Mote, P.W., Lundquist, J.D., 2010. Surface temperature lapse rates over complex
951 terrain: Lessons from the Cascade Mountains. *Journal of Geophysical Research:*
952 *Atmospheres* 115. <https://doi.org/10.1029/2009JD013493>

953 Mote, P.W., Li, S., Lettenmaier, D.P., Xiao, M., Engel, R., 2018. Dramatic declines in snowpack
954 in the western US. *npj Clim Atmos Sci* 1, 1–6. [https://doi.org/10.1038/s41612-018-0012-](https://doi.org/10.1038/s41612-018-0012-1)
955 1

956 Mudryk, L.R., Derksen, C., Kushner, P.J., Brown, R., 2015. Characterization of Northern
957 Hemisphere Snow Water Equivalent Datasets, 1981–2010. *Journal of Climate* 28, 8037–
958 8051. <https://doi.org/10.1175/JCLI-D-15-0229.1>

959 Musselman, K.N., Addor, N., Vano, J.A., Molotch, N.P., 2021. Winter melt trends portend
960 widespread declines in snow water resources. *Nat. Clim. Chang.* 11, 418–424.
961 <https://doi.org/10.1038/s41558-021-01014-9>

962 Musselman, K.N., Clark, M.P., Liu, C., Ikeda, K., Rasmussen, R., 2017. Slower snowmelt in a
963 warmer world. *Nature Clim Change* 7, 214–219. <https://doi.org/10.1038/nclimate3225>

964 Orlowsky, B., Bothe, O., Fraedrich, K., Gerstengarbe, F.-W., Zhu, X., 2010. Future Climates
965 from Bias-Bootstrapped Weather Analogs: An Application to the Yangtze River Basin.
966 *Journal of Climate* 23, 3509–3524. <https://doi.org/10.1175/2010JCLI3271.1>

967 Oyler, J.W., Dobrowski, S.Z., Ballantyne, A.P., Klene, A.E., Running, S.W., 2015. Artificial
968 amplification of warming trends across the mountains of the western United States.
969 *Geophysical Research Letters* 42, 153–161. <https://doi.org/10.1002/2014GL062803>

970 Pflug, J.M., Liston, G.E., Nijssen, B., Lundquist, J.D., 2019. Testing Model Representations of
971 Snowpack Liquid Water Percolation Across Multiple Climates. *Water Resources*
972 *Research* 55, 4820–4838. <https://doi.org/10.1029/2018WR024632>

973 Pflug, J.M., Margulis, S.A., Lundquist, J.D., 2022. Inferring watershed-scale mean snowfall
974 magnitude and distribution using multidecadal snow reanalysis patterns and snow pillow
975 observations. *Hydrological Processes* 36, e14581.

- 976 Pierce, D.W., Cayan, D.R., Thrasher, B.L., 2014. Statistical Downscaling Using Localized
 977 Constructed Analogs (LOCA). *Journal of Hydrometeorology* 15, 2558–2585.
 978 <https://doi.org/10.1175/JHM-D-14-0082.1>
- 979 Qian, Y., Ghan, S.J., Leung, L.R., 2010. Downscaling hydroclimatic changes over the Western
 980 US based on CAM subgrid scheme and WRF regional climate simulations. *International*
 981 *Journal of Climatology* 30, 675–693. <https://doi.org/10.1002/joc.1928>
- 982 Raleigh, M.S., Lundquist, J.D., Clark, M.P., 2015. Exploring the impact of forcing error
 983 characteristics on physically based snow simulations within a global sensitivity analysis
 984 framework. *Hydrol. Earth Syst. Sci.* 19, 3153–3179. [https://doi.org/10.5194/hess-19-](https://doi.org/10.5194/hess-19-3153-2015)
 985 [3153-2015](https://doi.org/10.5194/hess-19-3153-2015)
- 986 Rasmussen, R., Ikeda, K., Liu, C., Gochis, D., Clark, M., Dai, A., Gutmann, E., Dudhia, J.,
 987 Chen, F., Barlage, M., Yates, D., Zhang, G., 2014. Climate Change Impacts on the Water
 988 Balance of the Colorado Headwaters: High-Resolution Regional Climate Model
 989 Simulations. *Journal of Hydrometeorology* 15, 1091–1116. [https://doi.org/10.1175/JHM-](https://doi.org/10.1175/JHM-D-13-0118.1)
 990 [D-13-0118.1](https://doi.org/10.1175/JHM-D-13-0118.1)
- 991 Ray, P., Wi, S., Schwarz, A., Correa, M., He, M., Brown, C., 2020. Vulnerability and risk:
 992 climate change and water supply from California’s Central Valley water system. *Climatic*
 993 *Change* 161, 177–199. <https://doi.org/10.1007/s10584-020-02655-z>
- 994 Reynolds, D.S., Pflug, J.M., Lundquist, J.D., 2021. Evaluating Wind Fields for Use in Basin-
 995 Scale Distributed Snow Models. *Water Resources Research* 57, e2020WR028536.
 996 <https://doi.org/10.1029/2020WR028536>
- 997 Rhoades, A.M., Jones, A.D., Ullrich, P.A., 2018a. The Changing Character of the California
 998 Sierra Nevada as a Natural Reservoir. *Geophysical Research Letters* 45, 13,008–13,019.
 999 <https://doi.org/10.1029/2018GL080308>
- 1000 Rhoades, A.M., Ullrich, P.A., Zarzycki, C.M., 2018b. Projecting 21st century snowpack trends
 1001 in western USA mountains using variable-resolution CESM. *Clim Dyn* 50, 261–288.
 1002 <https://doi.org/10.1007/s00382-017-3606-0>
- 1003 Sheffield, J., Goteti, G., Wood, E.F., 2006. Development of a 50-Year High-Resolution Global
 1004 Dataset of Meteorological Forcings for Land Surface Modeling. *Journal of Climate* 19,
 1005 3088–3111. <https://doi.org/10.1175/JCLI3790.1>
- 1006 Siirila-Woodburn, E.R., Rhoades, A.M., Hatchett, B.J., Huning, L.S., Szinai, J., Tague, C., Nico,
 1007 P.S., Feldman, D.R., Jones, A.D., Collins, W.D., 2021. A low-to-no snow future and its
 1008 impacts on water resources in the western United States. *Nature Reviews Earth &*
 1009 *Environment* 2, 800–819.
- 1010 Sofaer, H.R., Barsugli, J.J., Jarnevich, C.S., Abatzoglou, J.T., Talbert, M.K., Miller, B.W.,
 1011 Morisette, J.T., 2017. Designing ecological climate change impact assessments to reflect
 1012 key climatic drivers. *Global Change Biology* 23, 2537–2553.
 1013 <https://doi.org/10.1111/gcb.13653>
- 1014 Srikrishnan, V., Lafferty, D.C., Wong, T.E., Lamontagne, J.R., Quinn, J.D., Sharma, S., Molla,
 1015 N.J., Herman, J.D., Srivier, R.L., Morris, J.F., Lee, B.S., 2022. Uncertainty Analysis in
 1016 Multi-Sector Systems: Considerations for Risk Analysis, Projection, and Planning for
 1017 Complex Systems. *Earth’s Future* 10, e2021EF002644.
 1018 <https://doi.org/10.1029/2021EF002644>
- 1019 Subyani, A.M., 2019. Climate variability in space-time variogram models of annual rainfall in
 1020 arid regions. *Arab J Geosci* 12, 650. <https://doi.org/10.1007/s12517-019-4836-8>

1021 Thornton, P.E., Shrestha, R., Thornton, M., Kao, S.-C., Wei, Y., Wilson, B.E., 2021. Gridded
1022 daily weather data for North America with comprehensive uncertainty quantification. *Sci*
1023 *Data* 8, 190. <https://doi.org/10.1038/s41597-021-00973-0>

1024 Thrasher, B., Wang, W., Michaelis, A., Melton, F., Lee, T., Nemani, R., 2022. NASA Global
1025 Daily Downscaled Projections, CMIP6. *Sci Data* 9, 262. [https://doi.org/10.1038/s41597-](https://doi.org/10.1038/s41597-022-01393-4)
1026 [022-01393-4](https://doi.org/10.1038/s41597-022-01393-4)

1027 Ullrich, P.A., Xu, Z., Rhoades, A. m., Dettinger, M. d., Mount, J. f., Jones, A. d., Vahmani, P.,
1028 2018. California’s Drought of the Future: A Midcentury Recreation of the Exceptional
1029 Conditions of 2012–2017. *Earth’s Future* 6, 1568–1587.
1030 <https://doi.org/10.1029/2018EF001007>

1031 Vano, J., Hammon, J., Gutmann, E., Wood, A., Mizukami, N., Clark, M., Pierce, D.W., Cayan,
1032 D., Wobus, C., Nowak, K., Arnold, J., 2020. Comparing Downscaled LOCA and BCSD
1033 CMIP5 Climate and Hydrology Projections: Release of Downscaled LOCA CMIP5
1034 Hydrology. U.S. Bureau of Reclamation.

1035 Walton, D.B., Hall, A., Berg, N., Schwartz, M., Sun, F., 2017. Incorporating Snow Albedo
1036 Feedback into Downscaled Temperature and Snow Cover Projections for California’s
1037 Sierra Nevada. *Journal of Climate* 30, 1417–1438. [https://doi.org/10.1175/JCLI-D-16-](https://doi.org/10.1175/JCLI-D-16-0168.1)
1038 [0168.1](https://doi.org/10.1175/JCLI-D-16-0168.1)

1039 Wayand, N.E., Hamlet, A.F., Hughes, M., Feld, S.I., Lundquist, J.D., 2013. Intercomparison of
1040 Meteorological Forcing Data from Empirical and Mesoscale Model Sources in the North
1041 Fork American River Basin in Northern Sierra Nevada, California. *Journal of*
1042 *Hydrometeorology* 14, 677–699. <https://doi.org/10.1175/JHM-D-12-0102.1>

1043 Wood, A.W., Leung, L.R., Sridhar, V., Lettenmaier, D.P., 2004. Hydrologic Implications of
1044 Dynamical and Statistical Approaches to Downscaling Climate Model Outputs. *Climatic*
1045 *Change* 62, 189–216. <https://doi.org/10.1023/B:CLIM.0000013685.99609.9e>

1046 Xue, Y., Janjic, Z., Dudhia, J., Vasic, R., De Sales, F., 2014. A review on regional dynamical
1047 downscaling in intraseasonal to seasonal simulation/prediction and major factors that
1048 affect downscaling ability. *Atmospheric Research* 147–148, 68–85.
1049 <https://doi.org/10.1016/j.atmosres.2014.05.001>
1050